https://doi.org/10.5194/essd-2026-719
Preprint. Discussion started: 28 September 2026

Open Access Earth System Science Data Discussions

ChinaTidalVSC: a 10 m wall-to-wall dataset of vegetation structural complexity in China's tidal wetlands derived from LiDAR-based relative entropy and AlphaEarth Foundation data

Guanpu Qi[1]†, Jiawei Wei[2]†, Zaizhou Xin[3], Longcheng Yao[1], Huilan Yuan[1], Ming Nie[1], Bo Li[1,4], Xiong Chen[2*], Jun Ma[1*]

[1] State Key Laboratory of Wetland Conservation and Restoration, National Observations and Research Station for Wetland Ecosystems of the Yangtze Estuary, Ministry of Education Key Laboratory for Biodiversity Science and Ecological Engineering, and Institute of Eco-Chongming, School of Life Sciences, Fudan University, # 2005 Songhu Road 10, Shanghai, 200438, China.

[2] School of Information Science and Engineering, Fudan University, # 2005 Songhu Road 10, Shanghai, 200438, China.

[3] Key Laboratory of Computational Physical Sciences (Ministry of Education), Institute of Computational Physical Sciences, State Key Laboratory of Surface Physics, and Department of Physics, Fudan University, Shanghai 200433, China.

[4] Ministry of Education Key Laboratory for Transboundary Ecosecurity of Southwest China; Yunnan Key Laboratory of Plant Reproductive Adaptation, Evolutionary Ecology and Centre for Invasion Biology, Institute of Biodiversity, School of Ecology and Environmental Science, Yunnan University, Kunming, 650504, China.

†These authors contributed to the work equally.

*Corresponding author

E-mail:

Jun Ma: **ma_jun@fudan.edu.cn**

Xiong Chen: **chenxiong@fudan.edu.cn**

Tel. Jun Ma: +86-21-31246690.

Tel. Xiong Chen: +86-21-65643231.

https://doi.org/10.5194/essd-2026-719
Preprint. Discussion started: 28 September 2026

Open Access Earth System Science Data Discussions

Abstract. Coastal wetlands are among the most valuable ecosystems globally, due to the high ecological function of their structurally complex vegetation communities. However, there remains a lack of vegetation structural complexity (VSC) indicators tailored for coastal wetland applications. Here, we developed a new VSC index, vegetation structure relative entropy (VSRE), based on a measure of the asymmetry of the difference between two probability distributions. While the currently used VSC index all fail to capture the discrete and continuous complexity gradients of coastal vegetation communities, VSRE demonstrated ideal performance in these applications, exhibiting strong robustness across varying point cloud densities. By applying this indicator to 1,337 LiDAR samples of natural coastal vegetation, we used Alpha Earth Foundation data and a deep learning model to create a seamless VSRE spatial map of coastal wetlands from 2017-2025 in China at high spatial resolution (10 m) and high accuracy (R^2 = 0.92). VSRE mapping provides crucial ecosystem structural information beyond vegetation classification data and conventional optical indices, highlighting the high spatial heterogeneity of VSC in coastal wetlands. This study offers a valuable foundation for prioritizing conservation areas and enhancing the resolution and accuracy of coastal zone ecological modeling.

https://doi.org/10.5194/essd-2026-719
Preprint. Discussion started: 28 September 2026

Open Access Earth System Science Data Discussions

1 Main

1.1 Introduction

Coastal wetlands, including saltmarshes, mangroves, and tidal flats, are among the world's most valuable ecosystems, rich in ecosystem services(Costanza et al., 1997). They not only fix and stabilize blue carbon at a rate far exceeding that of terrestrial ecosystems(Mcleod et al., 2011), which significantly mitigates climate change(Temmerman et al., 2013), but also defend shorelines from storms, purify water quality, and nurture fishery resources, thus bringing substantial benefits to coastal residents(He et al., 2025). In coastal ecosystems, these useful functions and services are realized by different functional groups of vegetation. The differences in their abilities to provide ecosystem services are determined by the structures of these groups(Lafond-Hudson and Sulman, 2023), that is, "structure determines function", which has been extensively confirmed by studies at scales from individuals to ecosystems(Holling, 1987; Chambers et al., 2007; Robinson et al., 2010; Loreau et al., 2001). Therefore, effectively and objectively quantifying vegetation structure is essential for more accurate estimation and prediction of ecosystem service provision in coastal wetlands.

Vegetation structural complexity (VSC), which refers to the three-dimensional organization and heterogeneity of vegetation elements, provides an important quantitative description of vegetation structure. By translating complex vegetation architecture into a comparable continuous variable, VSC offers a useful basis for analyzing structural variation across communities and ecosystems. Among the available methods for quantifying VSC, light detection and ranging (LiDAR) technology efficiently captures detailed structural information about ground features (Guo et al., 2020) and demonstrates superior capability for characterizing vegetation structure compared to traditional optical and radar

https://doi.org/10.5194/essd-2026-719
Preprint. Discussion started: 28 September 2026

methods(Dassot et al., 2011). LiDAR monitoring generates accurate spatial representations of plant structural elements as point clouds through high-precision, three-dimensional positioning measurements(Lohani and Ghosh, 2017). Numerous indicators of VSC have been developed over time using LiDAR data to quantify ecosystem structural attributes(Bergen et al., 2009). Examples of indices recognized as effective in quantifying vegetation structure include the horizontal structural index (canopy coverage)(Tang et al., 2019), the vertical structural index (foliage height diversity)(Macarthur and Macarthur, 1961), and integrated indices such as canopy rugosity(Parker and Russ, 2004), fractal dimension(Theiler, 1990), and canopy entropy(Liu et al., 2024). Among these, integrated VSC indices comprehensively quantify both vertical and horizontal structural attributes, exhibit broad applicability and representativeness, thereby dramatically enhancing our understanding of terrestrial ecosystems represented by forests (Ehbrecht et al., 2021).

However, most of these LiDAR-derived VSC metrics were developed and validated primarily in terrestrial ecosystems, especially forests (Coverdale and Davies, 2023). Whether they can reliably capture structural complexity in coastal wetlands remains unclear because the structural organization, environmental background, and observation conditions of coastal vegetation differ fundamentally from those of forest systems. There, vegetation is periodically inundated by tides and rooted in soft, muddy, or organic substrates with high water and salt content (He et al., 2025; Yando et al., 2023). It supports vegetation assemblages that often comprise open-canopy succulents, graminoids, and mangroves (Lafond-Hudson and Sulman, 2023). Relative to forests, these communities are typically shorter and more structurally compressed. The close juxtaposition of herbaceous and woody growth forms within a narrow vertical range can cause strong overlap among structural elements, reducing the ability of conventional

https://doi.org/10.5194/essd-2026-719
Preprint. Discussion started: 28 September 2026

VSC metrics to resolve subtle differences in three-dimensional organization (Taddeo et al., 2019). Tidal water surfaces further obscure low-stature vegetation and near-ground structure, increasing the likelihood of missing or unstable LiDAR returns (Moffett et al., 2015). These complications propagate from local measurements to regional inference: spaceborne optical and lidar observations cannot be consistently matched to low-tide conditions across repeated overpasses, and the fine-scale mosaics of vegetation, exposed mudflats, and water often result in severe mixed-pixel effects. Together, these features make VSC retrieval in coastal wetlands especially challenging in terms of sensitivity, robustness, and regional scalability.

An equally important limitation is the severe scarcity of VSC data and supporting covariates suitable for model development, accuracy validation, and spatial extrapolation in coastal ecosystems (Weilhoefer, 2011). First, coastal wetlands exhibit rapid dynamics, limited field accessibility, and extensive spatial distributions (Qi et al., 2026). These features increase acquisition costs and make it difficult to obtain medium- to high-density point clouds that can resolve vegetation's three-dimensional structure at ecologically meaningful scales, especially in publicly available datasets (e.g., OpenTopography, NEON, and NOAA Digital Coast) (Krishnan et al., 2011; Keller et al., 2008; Dobson, 1995). Second, many satellite remote sensing products that could potentially support VSC quantification were originally developed for terrestrial ecosystems, and their applicability in intertidal environments remains limited or insufficiently validated. This limitation is particularly relevant for spaceborne LiDAR products such as GEDI and ICESat-2, which still involve substantial uncertainty when applied to low-stature, open wetland vegetation strongly affected by tidal dynamics (Yu et al., 2026). Finally, environmental covariates used for large-scale VSC modeling and spatial extrapolation, including WorldClim and topographic variables

https://doi.org/10.5194/essd-2026-719
Preprint. Discussion started: 28 September 2026

(Fick and Hijmans, 2017; Kulp and Strauss, 2018), often face additional constraints in coastal areas, including insufficient spatial resolution, incomplete nearshore coverage, and large errors near land-sea boundaries. Together, these limitations have resulted in a lack of coastal-specific quantitative studies on VSC and of quality-controlled, standardized VSC products that can be used directly for modeling, validation, and regional extrapolation.

Based on the concept of relative entropy (RE, also known as the Kullback–Leibler divergence) (Cover and Thomas, 1991), we developed a LiDAR-derived index, vegetation structure relative entropy (VSRE), to quantify heterogeneity in local three-dimensional vegetation configurations. We first evaluated VSRE using UAV-LiDAR observations and field biomass measurements from 18 water-level-controlled experimental plots on Chongming Island, Shanghai, and compared its sensitivity and robustness with conventional LiDAR-derived VSC metrics across categorical and continuous complexity gradients and varying point-cloud densities. We then applied VSRE to 1,337 field LiDAR samples distributed along the coast of China to characterize structural variation among major coastal vegetation communities. Using the corresponding AlphaEarth Foundation embeddings, we trained a multilayer perceptron model to extrapolate sample-level VSRE to continuous 10 m coastal maps and systematically assessed the robustness of this extrapolation across training-sample size, point-cloud density, response range, and ecological support domains. Finally, we reconstructed annual VSRE from 2017 to 2025 to examine the spatial and temporal dynamics of vegetation structural complexity across China's coastal wetlands. Together, these analyses establish a framework for quantifying and mapping coastal VSC from local LiDAR observations to regional and multi-year scales.

1.2 Description

https://doi.org/10.5194/essd-2026-719
Preprint. Discussion started: 28 September 2026

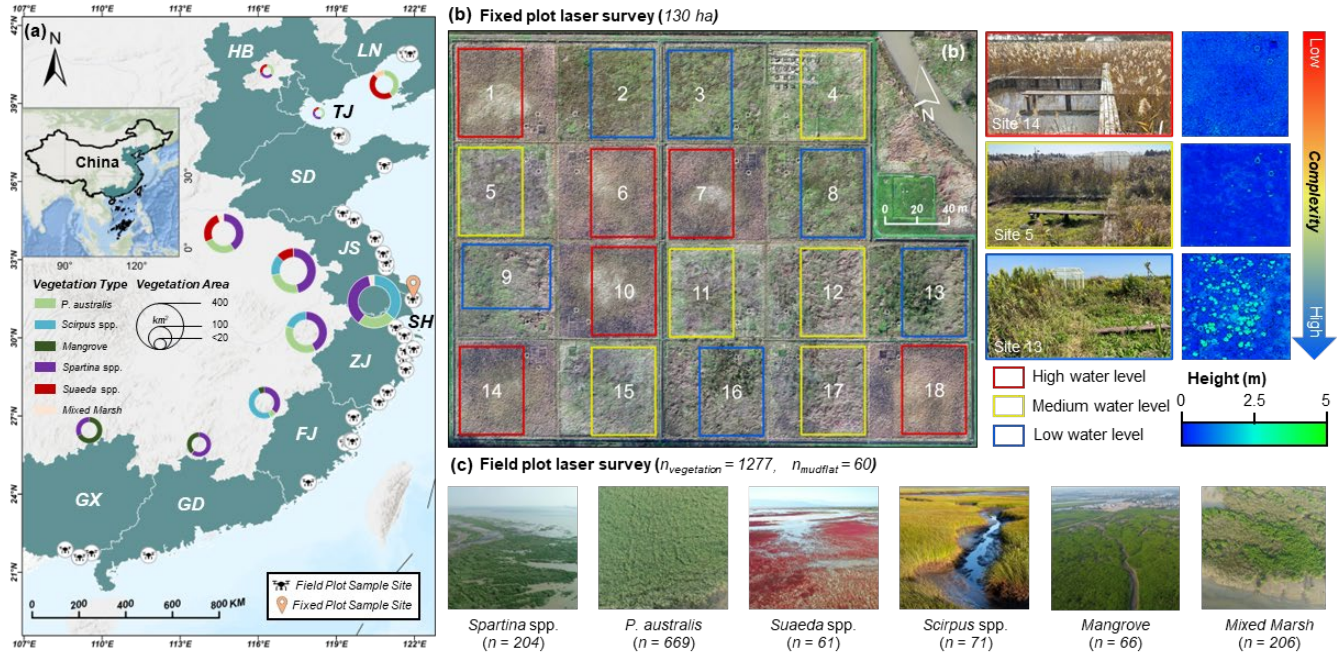

120 **Fig. 1 | Overview of fixed plots and spatial layout of field drone sampling sites. a**, Spatial distribution of all LiDAR sampling locations. Blue-green shading indicates sampled provinces, abbreviated with two-letter codes; drone icons represent the field LiDAR sampling sites, and the orange icon indicates the location of the fixed sampling site. **b**, LiDAR sampling conditions within fixed plots and primary vegetation communities surveyed. The LiDAR acquisition ranges under varying water levels are illustrated using three-color boxes, indicating that VSC decreases significantly as tidal levels rise. 125 Representative field photos and digital surface elevation profiles from three sampling points are displayed on the right. Field-collected LiDAR data encompass six typical coastal wetland vegetation types, including succulent herbs (*Suaeda* spp., *Scirpus* spp.), graminoid vegetation (*Phragmites australis*, *Spartina* spp.), mixed marsh communities, and tree-dominated communities (mangroves).

1.2.1 LiDAR data collection in the fixed plot

130 This study was based on the world's largest water-level-controlled wetland experimental plot, the Dongtan Ecosystem Experimental Plot (**121.94°E, 31.52°N**; **Fig. 1**). Established in 2018, this fixed plot has allowed vegetation to grow under natural coastal wetland conditions to date. The experimental setup includes three distinct water levels (-30 cm, 0 cm, and +30 cm), randomly distributed across a 130-hectare coastal wetland. The site was divided into 18 secondary plots, each measuring 60 × 60 meters, with two

https://doi.org/10.5194/essd-2026-719
Preprint. Discussion started: 28 September 2026

open-top chambers installed within each plot. Under these conditions, the vegetation communities developed distinct structural types: at the +30 cm tidal level, the community is dominated almost exclusively by *P. australis*; at the 0 cm level, diverse herbaceous species form mixed communities; and at the -30 cm level, mixed herbaceous species coexist with woody plants resembling mangrove structures. These treatment-induced differences provided three contrasting levels of vegetation structure for evaluating VSRE.

We conducted LiDAR surveys over the fixed plot using a DJI Matrice 300 RTK drone equipped with a DJI Zenmuse L1 LiDAR sensor. Each flight mission covered the entire experimental site to ensure accurate spatial matching. For UAV acquisition, the return mode was set to 3 returns to improve the point cloud's ability to capture vegetation elements at different vertical positions. Point cloud densities were controlled by adjusting flight height and overlap rate, targeting approximate densities of 50, 100, 250, 500, 1000, 1500, and 2000 pt m^{-2}. The datasets acquired at 50 and 100 pt m^{-2} were excluded because low return density, particularly over water-affected surfaces, resulted in insufficient representation of vegetation structure (**Supplementary Fig. 1**). Raw LiDAR data were processed in DJI Terra for stitching and denoising, and individual secondary plots were cropped to match the spatial extent of the ground survey plots. During cropping, we prioritized minimizing chamber inclusion while preserving all relevant vegetation features (specific cropping boundaries are shown in **Fig. 1b**).

1.2.2 LiDAR data collection in the field sites

We conducted field surveys along the mainland coast of China during the coastal vegetation growing season from July to August in 2022 and 2024, covering a latitudinal range from 21.5749°N to 40.9235°N (**Fig. 1a**). All surveys used the same UAV and LiDAR system as the fixed-plot experiment. A total of 81

https://doi.org/10.5194/essd-2026-719
Preprint. Discussion started: 28 September 2026


Open Access Earth System Science Data Discussions

LiDAR scanning missions were conducted across major coastal wetland regions, with optical imagery acquired simultaneously for vegetation identification and spatial delineation. LiDAR data were collected in three-return mode, and flight altitude, speed, and side overlap were adjusted to maintain a nominal acquisition density of >500 pt m^{-2}. Surveys were conducted under good visibility and low-tide conditions to maximize vegetation exposure. The accompanying optical imagery had a spatial resolution of approximately 0.5 m and was used to delineate vegetation patches and identify vegetation types during subsequent point-cloud cropping.

The stitched LiDAR datasets were further cropped into standardized samples according to vegetation-patch boundaries identified from the optical imagery. We extracted 1,337 coastal wetland samples of 25×25 m from the 81 flight-scale datasets. Each sample was assigned geographic coordinates and vegetation-type information, and adjacent samples were separated by at least 25 m to reduce spatial redundancy. Although the nominal acquisition density was maintained above 500 pt m^{-2}, realized sample-level PCD varied with local vegetation and surface conditions, ranging from 20.89 to 4,364.33 pt m^{-2}, with a mean of 790.22 pt m^{-2}.

In addition, we collected LiDAR data from 30 forest plots in Yunhe, Zhejiang Province (**Supplementary Table 1**) to provide an external structural reference for comparison with coastal vegetation. The same cropping procedure was applied to these data, with one 25 × 25 m sample retained from each forest plot. Forest-sample PCD ranged from 142.04 to 1,271.73 pt m^{-2}.

1.2.3 Fieldwork and quantitative VSC-proxy calculation

The three treatment-induced vegetation communities in the fixed plots were used to represent ordered levels of VSC based on their contrasting community composition and field-observed structural

https://doi.org/10.5194/essd-2026-719
Preprint. Discussion started: 28 September 2026

characteristics. To provide a continuous reference independent of the LiDAR-derived structural metrics, we further calculated a biomass-weighted Shannon index for each secondary plot. Biomass rather than individual abundance was used for weighting because the plots contained both herbaceous and woody species that differed markedly in individual density, body size, and contribution to three-dimensional vegetation structure. The biomass-weighted approach therefore reduced the disproportionate influence of the high numerical abundance of herbaceous individuals when characterizing community structural composition (Cousins, 1991).

Species-level biomass was expressed on a common area basis before calculation of the Shannon index. The resulting biomass density was assumed to represent herbaceous vegetation across the corresponding secondary plot. Specifically, we first summed the biomass of all herbaceous and tree species in each secondary plot to obtain the plot's total biomass ($Biomass_{total}$). The biomass of each species ($Biomass_i$) was then divided by $Biomass_{total}$ to calculate its relative biomass proportion (P_i) using Eq. (1). Finally, the Shannon diversity index (H) for each secondary plot was calculated based on the relative biomass proportion of each species using Eq. (2).

$$P_i = \frac{Biomass_i}{Biomass_{total}} \quad (1)$$

$$H = -\sum P_i \times \ln(P_i) \quad (2)$$

As environmental conditions across secondary plots were spatially similar, herbaceous vegetation exhibited relatively homogeneous growth patterns. Therefore, a tertiary sampling plot measuring 5 × 5 meters was established in the corner of each secondary plot to represent herbaceous vegetation for biomass assessment. In September 2024, we randomly deployed three 0.5 × 0.5 m quadrats within each

https://doi.org/10.5194/essd-2026-719
Preprint. Discussion started: 28 September 2026

tertiary plot to sample herbaceous plants for species identification. The sampled herbaceous vegetation was oven-dried at 70°C until a constant weight was achieved; this final weight was recorded as the biomass per unit area for herbaceous plants.

For woody plants growing in the center of the plots, considering the presence of sophisticated equipment monitoring soil respiration and vegetation carbon flux, we refrained from entering the plots for measurement to avoid interference and damage. Based on the highest point cloud density (2000 pt m^{-2}), we used a CHM-based individual-tree detection implemented in LiDAR360 software (Morsdorf et al., 2004), to segment individual trees within the fixed plots and assigned each segmented tree to its corresponding secondary plot (Fischer et al., 2019). The diameter at breast height (DBH) and crown height (CH) were recorded for each tree extracted using the segmentation algorithm. We measured the location, height, and DBH of 7 trees at the edge of the plots and compared them with vegetation parameters calculated after individual tree segmentation. The results showed that the errors were acceptable ($nRMSE_{CH}$ = 5.7%, $nRMSE_{DBH}$ = 2.4%). Furthermore, we identified tree species (mainly *Sapium sebiferum*) using UAV optical imagery and selected a matching allometric growth model to estimate biomass. Subsequently, we used a species-specific binary allometric growth model based on DBH and CH (Jucker et al., 2022) to calculate the total tree biomass of each secondary plot.

1.2.4 Development of vegetation structure relative entropy

VSRE was calculated from terrain-normalized LiDAR point clouds using a three-dimensional window-based framework. The normalized point cloud was first partitioned into horizontal analysis windows, each of which was further divided into a series of vertical subwindows. A normalized three-dimensional point-distribution histogram was constructed for each vertical subwindow, and RE was used to quantify

https://doi.org/10.5194/essd-2026-719
Preprint. Discussion started: 28 September 2026

differences among these distributions. The resulting divergence values were aggregated to characterize structural heterogeneity within each horizontal window and subsequently across the entire sample.

We first normalize the density distributions within sliding windows to mitigate potential biases, thereby reducing the influence of local anomalies (e.g., occlusions, water bodies, or data gaps) and global variations in point density. The VSRE is then computed on these normalized distributions to quantify spatial heterogeneity in a standardized manner. By adjusting scale-specific sliding intervals and window sizes, our algorithm enhances the continuity of local features, enabling a spatially explicit assessment of VSC.

Let $\tilde{\mathcal{P}} = \{(x_i, y_i, z_i - \hat{z_i})\}_{i=1}^{N}$ represent the terrain-eliminated point cloud data. Where $\hat{z} = f(x, y)$ is the estimated terrain height. To capture local variations in point density and spatial structure, the terrain-normalized point cloud is divided into 3D windows. Let $\mathcal{W}(\mathrm{x}, \mathrm{y}, \mathrm{z})$ be a window in space with ranges $(\mathrm{L_x}, \mathrm{L_y}, \mathrm{L_z})$. The segmentation of $\tilde{\mathcal{P}}$ is performed using a sliding window approach, where the window boundaries are defined as:

$$\begin{cases} x \in [m_x \cdot (1-o) \cdot L_x, (m_x+1) \cdot (1-o) \cdot L_x] \\ y \in [m_y \cdot (1-o) \cdot L_y, (m_y+1) \cdot (1-o) \cdot L_y] \\ z \in [m_z \cdot L_z, (m_z+1) \cdot L_z] \end{cases} \quad (3)$$

Where $m_x, m_y, m_z = [1, jix., m_{x,y,z}^{max}] \in Z^+$ represent the sliding indices. To further mitigate the impact of water bodies and cracks on the horizontal plane, an overlap factor $o \in [0,1]$ is introduced. This factor facilitates information sharing between adjacent windows, enhancing the continuity of local features and reducing the boundary effect between windows. By setting windows at different scales, local structural features can be extracted at various spatial resolutions, thus improving the representation of vegetation structure.

https://doi.org/10.5194/essd-2026-719
Preprint. Discussion started: 28 September 2026

To ensure robustness against point cloud variations, the distribution of points within each window is modeled through a 3D histogram. Furthermore, the window is uniformly divided into voxels b with side lengths $\Delta x, \Delta y, \Delta z$. For the point cloud data $\mathcal{P}_w$ within the window, the 3D histogram is defined as:

$$H(i,j,k) = \frac{|\{(x_n, y_n, z_n) | (x_n, y_n, z_n) \in b_{ijk}\}|}{|\mathcal{P}_w|} \quad (4)$$

The histogram is then normalized (Π) to obtain the spatial distribution of points within the current window for subsequent quantification of vegetation structure. We use the RE to measure distributional differences across windows. For two distributions, Φ and Ψ representing different sub-windows, the RE for discrete distributions is defined as:

$$RE(\Phi||\Psi) = \sum_{i,j,k} \Phi_{ijk} \log \frac{\Phi_{ijk} + \epsilon}{\Psi_{ijk} + \epsilon} \quad (5)$$

To ensure numerical stability in RE computation and avoid divergence caused by empty voxels or extremely sparse regions (where $\log(0) \to \infty$), we introduce a minimal positive constant ϵ to all probability distributions, thereby eliminating zero-probability elements. In our implementation for field data, we set $\epsilon = 1e - 43.43$ to standardize the structural complexity metric, constraining all RE scores to a comparable range of 0-100. Although RE is inherently asymmetric and nonlinear, the VSRE maintains interpretability by averaging window-level scores. Given that RE's sensitivity to distributional differences follows an exponential differential form ($\log(p/q)$), complexity growth exhibits sub-exponential scaling, meaning a doubling of VSRE scores reflects a substantial increase in structural heterogeneity (**Supplementary Fig. 5**).

https://doi.org/10.5194/essd-2026-719
Preprint. Discussion started: 28 September 2026

Open Access Earth System Science Data Discussions

For each vertical layer, the RE is computed for all window pairs, yielding the structural diversity score for the current horizontal block. The overall structural complexity score is obtained by averaging the structural diversity scores across all horizontal regions:

$$VSRE = \frac{1}{m_x^{max} \cdot m_y^{max}} \sum^{m_x^{max}} \sum^{m_y^{max}} \frac{1}{m_z^{max} \cdot (m_z^{max} - 1)} \sum_{\substack{i,j=1 \\ i \neq j}}^{m_z^{max}} KL(\Pi_i || \Pi_j) \quad (6)$$

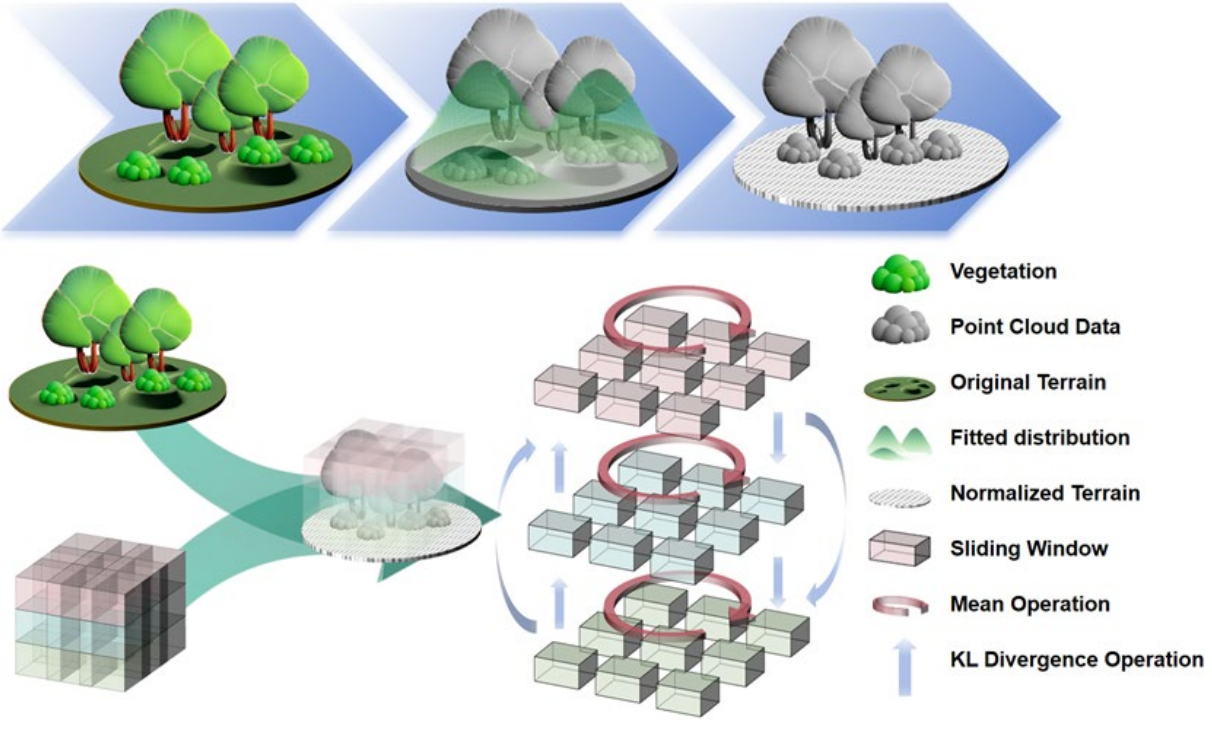

Fig. 2 | Framework of the vegetation 3D structural quantification method based on a sliding window and RE. The figure illustrates key technical processes from raw point clouds to vegetation structural parameter extraction: raw point cloud data undergo terrain surface fitting and normalization to eliminate topographic relief; 3D sliding windows segment the space to construct local voxel probability distributions; RE quantifies spatial heterogeneity by computing RE between adjacent window distributions, characterizing VSC.

1.2.5 Comparison analysis with existing VSC metrics

https://doi.org/10.5194/essd-2026-719
Preprint. Discussion started: 28 September 2026

To evaluate whether VSRE captured structural information beyond conventional LiDAR-derived metrics, we compared it with five representative VSC metrics describing complementary dimensions of vegetation structure: mean vegetation height, canopy cover (Atkins et al., 2018), foliage height diversity (FHD) (Macarthur and Macarthur, 1961), canopy rugosity(Parker and Russ, 2004), and canopy entropy (CE) (Liu et al., 2022). These metrics represent vertical development, horizontal occupancy, vertical heterogeneity, canopy-surface variation, and integrated three-dimensional occupancy, respectively. Detailed definitions and calculation procedures are provided in **Supplementary Text 2**.

All conventional metrics and VSRE were calculated for the same LiDAR samples and spatial extents and were evaluated using the same statistical framework. This design allowed direct comparison of their sensitivity to treatment-derived VSC differences, continuous structural variation, and changes in PCD.

1.2.6 Mapping the VSRE in coastal China

To extend VSRE estimation from sample-based measurements to wall-to-wall mapping, we used the recently released Alpha Earth Foundation (AEF) dataset(Brown et al., 2025). AEF provides annual, seamless 64-dimensional spatial embeddings at a spatial resolution of 10 m. The embedding space integrates information from multiple Earth observation sources and represents multidimensional land-surface characteristics in a normalized latent feature space. We extracted all 64 AEF embedding dimensions (A00–A63) corresponding to the locations of the 1,337 coastal LiDAR samples and used them as predictor variables for VSRE extrapolation.

For spatial modelling, VSRE was calculated using a maximum vertical extent of 5 m and a vertical interval of 0.5 m to enhance sensitivity to structural variation within the vertically compressed vegetation layer characteristic of most coastal wetlands. The VSRE scaling parameter was further set so that the

https://doi.org/10.5194/essd-2026-719
Preprint. Discussion started: 28 September 2026

resulting index was normalized to an interpretable range of approximately 0–100. Before model development, robust z-scores were calculated from the VSRE distribution to identify potentially anomalous observations. Samples with $|Z| > 2.5$ were subjected to quality screening, and 64 samples showing unreliable VSRE estimates associated with data-quality issues were excluded. This procedure retained 1,273 quality-controlled samples for subsequent modelling, with VSRE values ranging from 4.358 to 77.289.

We compared statistical, machine-learning, and deep-learning regression models using 10-fold cross-validation, with MAE as the model-selection criterion (**Supplementary Table 4**). MLP achieved the lowest cross-validation MAE and was therefore selected for subsequent spatial modelling and robustness analyses(Pinkus, 1999). The MLP consisted of 64 input nodes followed by three hidden layers containing 256, 128, and 64 nodes, respectively. Each hidden layer was sequentially followed by batch normalization, a rectified linear unit (ReLU) activation function, and dropout with a rate of 0.1. A single linear output node was used to predict VSRE. The model was trained using MAE as the loss function and the Adam optimizer, with a learning rate of 0.0005, a batch size of 64, and 200 training epochs. The random seed was fixed at 42.

The predictive performance of the full model was evaluated using random sample-level 10-fold cross-validation. The 1,273 samples were randomly shuffled and divided into ten folds. In each iteration, nine folds were used for model training and the remaining fold for validation, such that every sample received one strictly out-of-fold (OOF) prediction from a model that had not been trained on that sample. Overall model performance was calculated from the pooled OOF predictions across all ten folds. Model

https://doi.org/10.5194/essd-2026-719
Preprint. Discussion started: 28 September 2026

performance was quantified using the coefficient of determination (R^2), MAE, root mean square error (RMSE), range-normalized RMSE (nRMSE), and prediction bias.

Model interpretation was conducted using SHapley Additive exPlanations (SHAP) within the same OOF framework (Chen et al., 2023). The ten models generated during random 10-fold validation were retained, and each sample was explained only by the model for which that sample belonged to the held-out fold. SHAP values were calculated using GradientExplainer, with 100 samples selected from the corresponding training fold as the background dataset and 200 approximation samples used for each explanation. Global feature importance was quantified as the mean absolute OOF SHAP value across all samples. The 20 most influential AEF dimensions were ranked by global importance, and dependence relationships between feature values and SHAP values were examined for the eight leading dimensions.

1.2.7 Robustness assessment of VSRE spatial extrapolation

We evaluated the robustness of VSRE spatial extrapolation to variation in training sample size, VSRE support range, ecological composition, and PCD. Because several experiments required stratified subsampling to balance ecological or acquisition conditions, we first quantified the effect of training sample size to distinguish genuine support-domain sensitivity from performance changes caused by reduced data availability. All experiments used the MLP architecture and training parameters described in **Section 1.2.6**.

Sensitivity to training sample size was evaluated using a nested learning-curve design with a fixed external test set. A total of 254 samples were selected by complete base plots as the external test set, while the remaining 1,019 samples formed the training pool, with no base-plot overlap between the two sets. Nested training subsets containing 15%, 25%, 40%, 60%, 80%, and 100% of the training pool were

https://doi.org/10.5194/essd-2026-719
Preprint. Discussion started: 28 September 2026


Open Access Earth System Science Data Discussions

constructed, corresponding to 153, 255, 408, 611, 815, and 1,019 samples, respectively. Sampling was stratified by vegetation type, acquisition year, VSRE decile, and log-transformed PCD decile, while ensuring representation of each training base plot from the smallest subset onward. Within each repetition, smaller subsets were strict subsets of larger subsets. Each sample-size level was repeated ten times, and five independently trained models were averaged to predict the same fixed external test set. Performance at each level was compared with the corresponding 100% training-pool baseline from the same repetition.

Sensitivity to the VSRE support range was evaluated using global and composition-conditioned designs. In the global design, samples were divided into ten deciles according to VSRE across the complete dataset, retaining the observed covariation of VSRE with vegetation composition and PCD. In the conditioned design, PCD was first divided into three relative classes within each vegetation type, after which samples were ranked by VSRE within each vegetation-type × PCD stratum and assigned to ten composition-matched VSRE classes of 122 samples each. For both designs, we evaluated the full-support baseline, ten scenarios in which one VSRE decile was withheld from training, and nine scenarios in which two adjacent deciles were withheld. Five-fold validation was grouped by base plot. For each withheld interval, the reduced-support model and full-support baseline were evaluated on the same held-out samples, allowing direct comparison of prediction performance under identical test conditions.

Sensitivity to ecological support was first evaluated at the individual vegetation-type level using a balanced dataset. Within each vegetation type, samples were divided into relative VSRE tertiles, followed by three conditional PCD classes within each vegetation-type × VSRE stratum. Six samples were randomly selected from each resulting combination, yielding 54 samples per class and 378 samples in total. A model trained with all classes served as the paired baseline, after which each class was

https://doi.org/10.5194/essd-2026-719
Preprint. Discussion started: 28 September 2026

sequentially excluded from training and treated as unseen during prediction. Five-fold validation was grouped by base plot, and performance was evaluated on the excluded class relative to the paired full-composition baseline.

We further evaluated ecological support at a broader functional-group level using the same stratified balancing principle. Four groups containing 54 samples each were constructed, yielding 216 samples in total. The tall-graminoid group contained 18 samples each from mixed marsh, *P. australis*, and *Spartina* spp.; the low-stature herbaceous group contained 27 samples each from *Scirpus* spp. and *Suaeda* spp.; mangrove and tidal-flat groups each contained 54 samples. A full-composition model served as the paired baseline, after which each group was sequentially withheld from training and predicted as an unseen group using five-fold validation grouped by base plot.

Sensitivity to PCD was evaluated using a matched design that controlled for covariation with vegetation composition and VSRE. Within each vegetation type, samples were first divided into three relative VSRE classes and subsequently ranked by PCD within each vegetation-type × VSRE stratum. Samples were then assigned to five conditional PCD classes and downsampled according to the least-represented class, producing a matched dataset of 1,240 samples with 248 samples per PCD class and equivalent vegetation and VSRE-stratum composition among classes. Five-fold OOF prediction using the complete matched dataset served as the baseline. Each conditional PCD class was then sequentially withheld from training and treated as unseen during prediction. The resulting Q1–Q5 classes therefore represent relative PCD ranks conditional on vegetation type and VSRE.

Across all robustness analyses, performance was quantified using R^2, MAE, RMSE, nRMSE, and prediction bias. nRMSE was calculated by dividing RMSE by the observed VSRE range of 72.9313 and

https://doi.org/10.5194/essd-2026-719
Preprint. Discussion started: 28 September 2026

expressing the result as a percentage. For **Fig. 7**, sensitivity was summarized as the increase in MAE relative to the corresponding full-support baseline, with positive values indicating reduced prediction performance after removal of training support. Uncertainty was expressed as the standard deviation across the five validation folds for the VSRE-range, ecological-support, and PCD experiments, and across the ten nested-sampling repetitions for the training-sample-size experiment.

1.2.8 Spatiotemporal analysis of VSRE across coastal China

To characterize temporal variation in coastal vegetation structure, the final MLP model was applied to annual AEF embeddings from 2017 to 2025 to generate annual VSRE maps at 10 m resolution. The same model structure and VSRE response definition used for spatial extrapolation were retained across all years to ensure temporal consistency.

For regional trend analysis, annual VSRE values were aggregated within 0.5° × 0.5° coastal grid cells. For each valid grid cell, the annual mean VSRE from 2017 to 2025 was used to calculate Sen's slope, and the significance of monotonic temporal trends was evaluated using the Mann–Kendall test. Grid cells were classified as increasing or decreasing according to the sign of Sen's slope and as significant or non-significant using a threshold of $P < 0.1$.

To examine temporal changes in VSRE while reducing confounding from vegetation-type transitions, we further identified locations that were consistently classified as the same vegetation type throughout 2017–2022 using the annual vegetation maps of previous studies (Qi et al., 2026). A total of 103,017 locations met this criterion. These locations were grouped according to their stable 2017–2022 vegetation identity, and their annual VSRE values were tracked from 2017 to 2025. Because annual vegetation

https://doi.org/10.5194/essd-2026-719
Preprint. Discussion started: 28 September 2026

classifications were unavailable after 2022, group labels for 2023–2025 represent historical pre-2023 vegetation identity.

1.2.9 Overall workflow

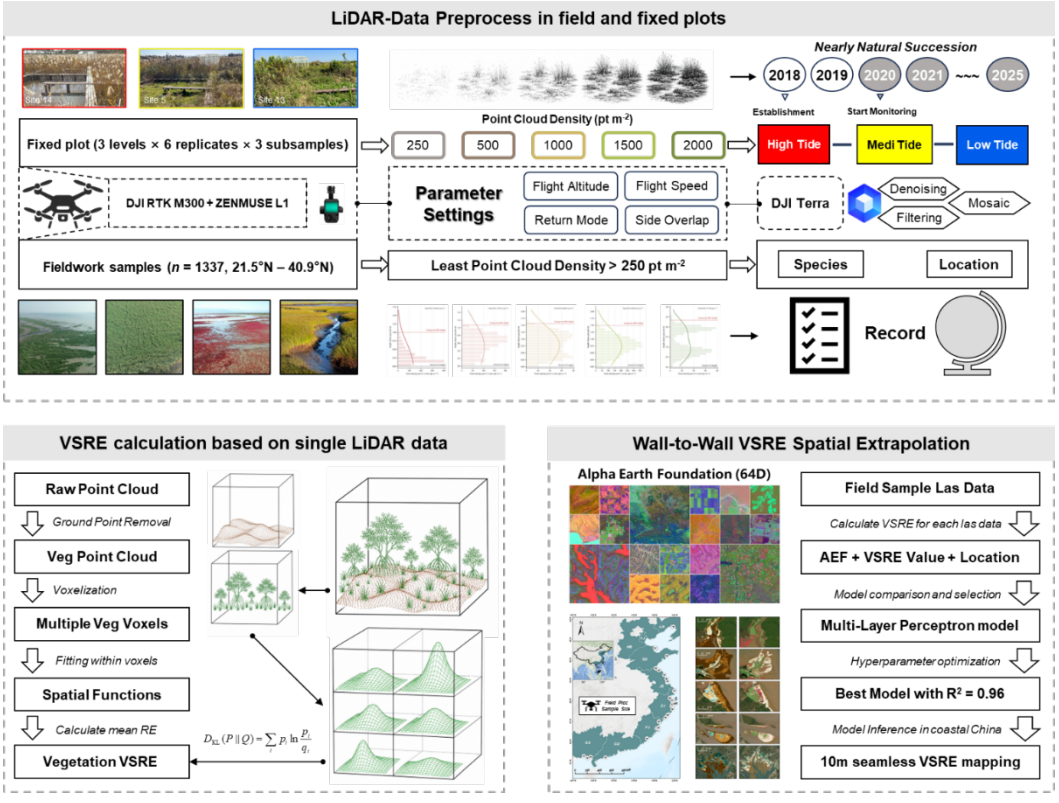

Fig. 3 | Overall workflow of this study.

1.2.10 Statistical analysis and software used

Nonparametric statistical tests were used to evaluate differences in VSRE and the conventional structural metrics among the treatment-derived VSC groups. At each PCD level, overall differences among the low-, medium-, and high-VSC groups were assessed using Kruskal–Wallis tests. When significant differences were detected, pairwise comparisons were performed using Dunn's post hoc tests with Benjamini–Hochberg correction for multiple comparisons. The same procedure was applied after pooling samples across all PCD levels to evaluate differences among VSC groups under mixed PCD conditions.

https://doi.org/10.5194/essd-2026-719
Preprint. Discussion started: 28 September 2026


Open Access Earth System Science Data Discussions

Relationships between the biomass-weighted Shannon index and LiDAR-derived structural metrics were evaluated using separate linear regression models at each PCD level. The biomass-weighted Shannon index was treated as the explanatory variable and each structural metric as the response variable, providing a continuous evaluation of metric sensitivity to variation in VSC.

The statistical analyses described in this section were performed using R (Version 4.3.2). Figures were generated using Origin Pro 2023 (Version 9.0.0.87), ArcMap Desktop 10.8 (Esri), Adobe Photoshop (Version 25.0, 2023), and Adobe Illustrator (Version 27.9, 2023).

https://doi.org/10.5194/essd-2026-719
Preprint. Discussion started: 28 September 2026


Open Access Earth System Science Data Discussions

1.3 Results

1.3.1 Effectiveness of VSRE in quantifying coastal VSC

To evaluate the performance of VSRE in coastal wetlands, we used the 18 fixed plots in which the water-level treatments generated three ordered levels of VSC. The low-, medium-, and high-VSC groups were defined according to their community composition and field-observed structural characteristics (**Fig. 1b)**, and this ordering was independently supported by the biomass-weighted Shannon index (**Supplementary Fig. 2**). For the fixed-plot analysis, the maximum box height and Z-direction step size were set to 5 and 0.5 m, respectively, based on the observed vegetation height range; the remaining hyperparameters were optimized by grid search (**Supplementary Figs. 3 and 4**).

VSRE consistently distinguished the three VSC groups across all five tested point cloud density (PCD) levels, ranging from 250 to 2000 pt m^{-2} (**Fig. 4a**). At each PCD, VSRE increased monotonically from the low- to medium- and high-VSC groups, and all three groups were significantly separated (Kruskal–Wallis, $P < 0.001$; Dunn's post hoc tests). This ordering and statistical separation were maintained despite an eightfold difference in PCD, indicating that VSRE is robust to substantial variation in sampling density within the tested range.

The same pattern was retained when samples from all five PCD levels were pooled. The low-, medium-, and high-VSC groups remained significantly differentiated and preserved the expected ordering ($P < 0.001$; **Fig. 4b**). VSRE also captured continuous variation in VSC. Using the biomass-weighted Shannon index as a quantitative proxy, VSRE showed significant positive relationships with VSC at all five PCD levels, with R^2 values ranging from 0.57 to 0.71 (all $P < 0.001$; **Fig. 4c**). Together, these categorical, mixed-PCD, and continuous-gradient evaluations show that VSRE captures variation in

https://doi.org/10.5194/essd-2026-719
Preprint. Discussion started: 28 September 2026

coastal vegetation structure while maintaining stable performance across substantial differences in point cloud density.

In comparison, the five conventional LiDAR-derived metrics did not consistently recover the expected VSC ordering or continuous structural gradient across PCD levels, whereas VSRE retained stable performance across the categorical, mixed-PCD, and continuous evaluations (**Supplementary Text 3; Supplementary Figs. 7–9**).

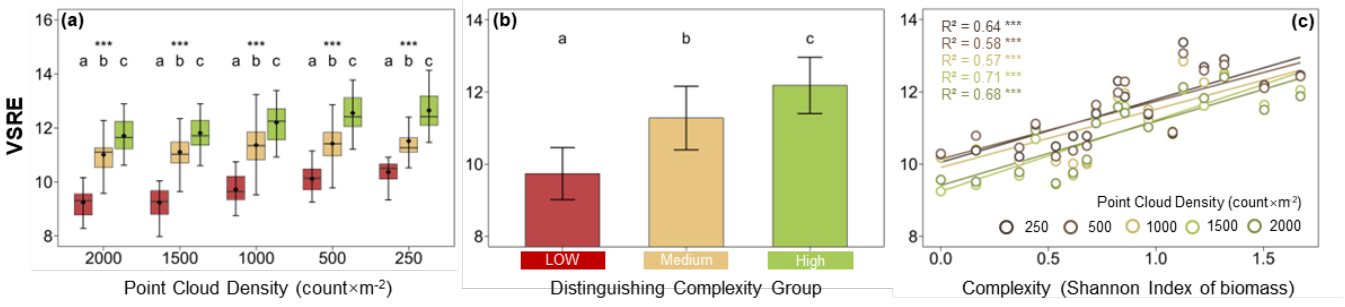

Fig. 4 | Effectiveness and robustness of VSRE in quantifying coastal wetland VSC across point cloud densities. a, VSRE distributions for low-, medium-, and high-VSC groups at five point cloud densities (PCDs; 250, 500, 1000, 1500, and 2000 pt m^{-2}). Boxplots show the median, interquartile range, and non-outlier range; outliers are not displayed, and black diamonds denote group means. Differences among VSC groups were tested separately at each PCD using Kruskal–Wallis tests followed by Dunn's post hoc tests with Benjamini–Hochberg correction. Different letters indicate significant pairwise differences, and *** indicates $P < 0.001$ for the overall Kruskal–Wallis test. **b**, VSRE values after pooling samples across all five PCD levels. Bars show group means and error bars indicate standard deviations. Different letters indicate significant pairwise differences among VSC groups after the Kruskal–Wallis and Dunn's post hoc tests. **c**, Relationships between VSRE and the biomass-weighted Shannon index used as a continuous proxy for VSC. Each circle represents one plot-level UAV-LiDAR sample, and separate linear regressions were fitted for each PCD. R^2 values are shown for each regression; all relationships were significant at $P < 0.001$. Colors in a and b indicate low (red), medium (yellow), and high (green) VSC, while colors in c denote the five PCD levels.

1.3.2 Structural diversity of natural vegetation in coastal China

https://doi.org/10.5194/essd-2026-719
Preprint. Discussion started: 28 September 2026

We applied VSRE to 1,337 LiDAR samples collected across coastal China. For this community-level comparison, a maximum vertical extent of 10 m and a vertical interval of 0.5 m were used to encompass the full height range of the sampled coastal vegetation, including mangroves.

VSRE differed significantly among coastal vegetation communities ($P < 3.33 \times 10^{-111}$; **Fig. 5**). Mangroves exhibited the highest VSRE, with a median of 22.70, significantly exceeding all other vegetation types. *P. australis*, mixed marsh, and *Spartina* spp. showed intermediate values, with median VSRE values of 19.32, 13.19, and 11.49, respectively. *Scirpus* spp. and *Suaeda* spp. exhibited the lowest median VSRE values, at 7.91 and 5.77, respectively, with no significant difference between them.

Vegetation types with higher median VSRE also tended to show greater among-sample variability, indicating stronger spatial variation in structural complexity within these vegetation classes. The coastal vegetation samples generally exhibited lower VSRE than the supplementary forest reference samples, which had a mean VSRE of 39.11 (**Supplementary Table 1**). Sensitivity analysis further showed that the relative differences among coastal vegetation communities were maintained across the tested values of the smoothing constant (**Supplementary Fig. 5**).

https://doi.org/10.5194/essd-2026-719
Preprint. Discussion started: 28 September 2026

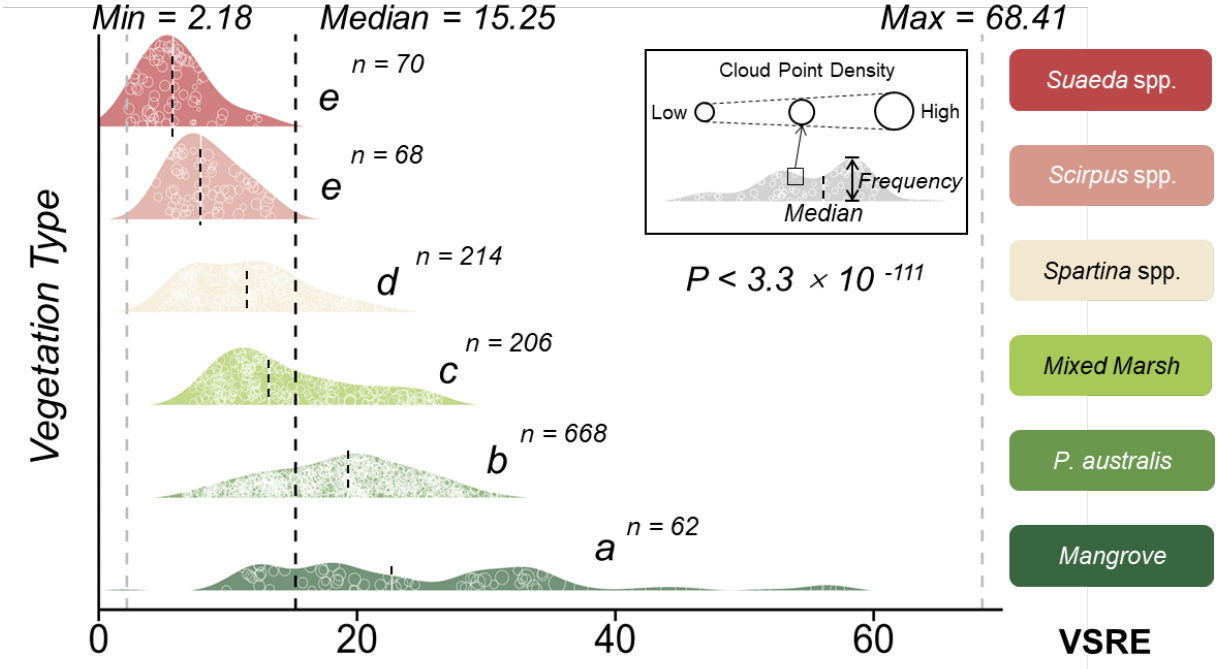

Fig. 5 | VSRE distributions across natural coastal vegetation communities. The frequency distributions of VSRE values for different plant communities are shown. Black dashed lines on a white background indicate the median VSRE for each vegetation community. White circles within the distribution curves represent the density of the sample point clouds. The overall median VSRE across all samples is also visualized with a black dashed line, while the grey curves indicate the maximum and minimum values observed. Kruskal–Wallis tests followed by Dunn's post hoc tests were used to assess significant differences in VSRE among vegetation communities.

1.3.3 Predictive performance and interpretation of AlphaEarth-based VSRE extrapolation

After quality control, 1,273 LiDAR samples were retained for spatial extrapolation. The MLP model reproduced the observed variation in VSRE with high accuracy under 10-fold out-of-fold (OOF) prediction (**Fig. 6a**), achieving an R^2 of 0.921, an MAE of 3.070, and an RMSE of 3.937. Predicted values closely followed the 1:1 relationship across the main observed VSRE range, although prediction dispersion increased slightly toward the upper end of the distribution, where observations were relatively sparse.

https://doi.org/10.5194/essd-2026-719
Preprint. Discussion started: 28 September 2026


Open Access Earth System Science Data Discussions

OOF SHAP analysis showed that model prediction was driven by a subset of AlphaEarth embedding dimensions, while predictive information remained distributed across multiple features (**Fig. 6b**). A34 showed the highest mean absolute SHAP value, followed by A35, A43, A54, A51, A39, A27, and A48. Previous interpretability analyses of AlphaEarth embeddings provide physical or ecological associations for several of these leading dimensions(Rahman, 2026). A34 has been associated with elevation, A43 with soil pH, and A48 with vegetation properties, while A27 has been tentatively associated with vegetation-related information. Clear physical interpretations have not yet been assigned to A35, A54, A51, or A39. The presence of both vegetation- and environment-associated dimensions among the leading predictors suggests that the model used multiple components of the information encoded by AEF to predict VSRE.

The SHAP dependence patterns showed clear and largely monotonic relationships between the leading embedding dimensions and model predictions (**Fig. 6c**). Increasing values of A34, A43, A48, and A27 were associated with progressively more positive contributions to predicted VSRE, whereas A35, A51, A54, and A39 showed the opposite response. Among the physically interpretable dimensions, the positive response of A48 indicates that vegetation-related information encoded by AlphaEarth contributed positively to VSRE prediction. Terrain- and soil-associated dimensions A34 and A43 also showed consistent positive responses, suggesting that the model incorporated environmental information associated with spatial variation in vegetation structure. Across the eight leading dimensions, the SHAP responses changed gradually over their observed feature ranges without pronounced discontinuities, indicating that their contributions to VSRE prediction were primarily continuous rather than dominated by isolated threshold effects.

https://doi.org/10.5194/essd-2026-719
Preprint. Discussion started: 28 September 2026

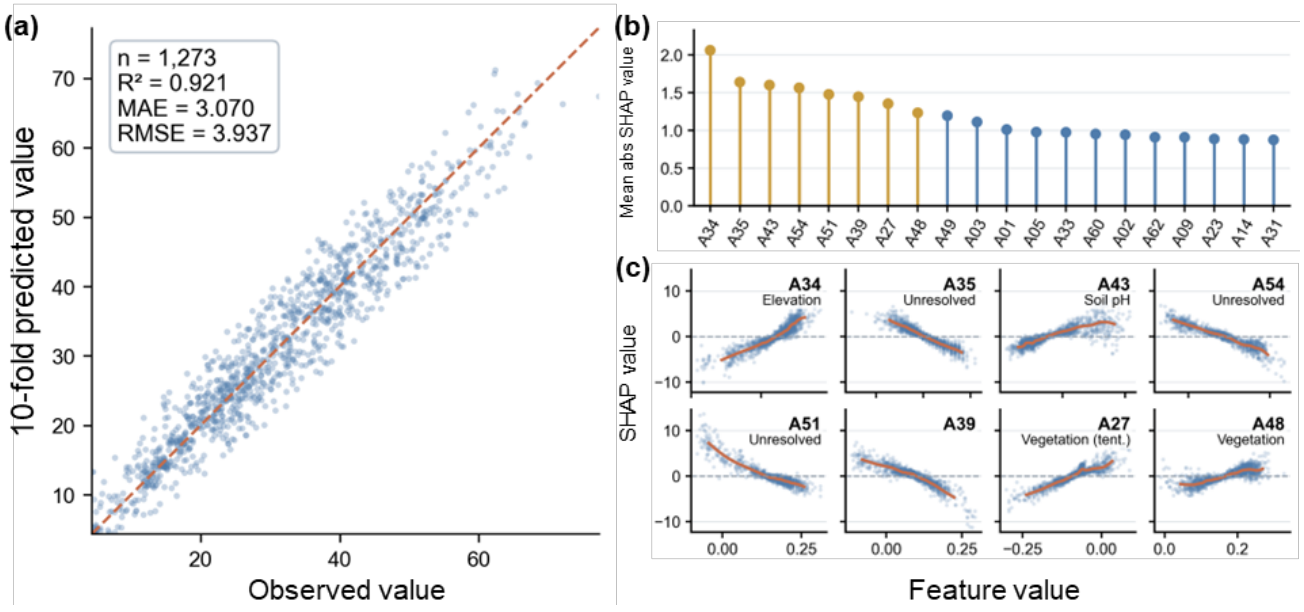

Fig. 6 | Predictive performance and AlphaEarth-based interpretation of the VSRE model. a, Relationship between observed VSRE and 10-fold out-of-fold (OOF) predictions. The orange dashed line denotes the 1:1 relationship; the inset reports the sample size, coefficient of determination (R^2), mean absolute error (MAE) and root mean square error (RMSE). **b**, Global importance of the 20 leading AlphaEarth embedding dimensions, quantified as the mean absolute OOF SHAP value. The eight most influential dimensions are highlighted in gold. **c**, SHAP dependence patterns for the eight leading dimensions. Points represent sample-level OOF SHAP values, orange curves show smoothed trends through quantile-binned means, and grey dashed lines indicate zero contribution. Descriptive labels denote proposed physical or ecological associations; uncertain dimensions remain marked as unresolved or tentative.

1.3.4 Robustness of VSRE spatial extrapolation across training and support domains

The VSRE prediction model showed substantial tolerance to reductions in training sample size (**Fig. 7a**). Relative to the model trained with the complete training pool, prediction error changed only slightly when 40–80% of the training samples were retained, and remained comparatively low when the training set was further reduced to 25%. A pronounced increase in MAE occurred only when 15% of the original training pool was retained, reaching approximately 16 VSRE units above the full-data baseline. This broad tolerance to sample reduction indicates that moderate downsampling itself contributed little to model-

https://doi.org/10.5194/essd-2026-719
Preprint. Discussion started: 28 September 2026

performance changes over most of the tested range, providing a basis for the balanced subsampling used in the subsequent sensitivity analyses.

Prediction was also generally insensitive to variation in LiDAR point-cloud density after differences in vegetation composition and VSRE were controlled (**Fig. 7b**). Withholding the Q1–Q4 conditional density classes produced little change in MAE relative to the matched baseline, whereas exclusion of the highest relative density class (Q5) resulted in only a modest increase in prediction error. Thus, within the density range represented by the field observations, variation in PCD had substantially less influence on extrapolation accuracy than the major reductions in training support examined below.

Sensitivity to the observed VSRE range depended strongly on whether associated differences in vegetation composition and PCD were controlled (**Fig. 7c,d**). Under the global percentile design, withholding most intermediate VSRE intervals caused relatively small increases in MAE, whereas larger performance losses occurred toward the edges of the observed VSRE distribution, particularly when broader 20% intervals were excluded. The associated variability among folds also increased near the upper end of the VSRE range. After conditioning the percentile classes on vegetation type and PCD, these effects were substantially reduced: MAE changes for most withheld intervals remained close to the full-range baseline, with appreciable increases confined mainly to the highest VSRE ranges. These results indicate that much of the apparent sensitivity to the global VSRE range was associated with concurrent changes in ecological and acquisition composition, while extrapolation became more difficult primarily near the sparsely represented extremes of the response distribution.

Ecological support showed stronger and more heterogeneous effects on prediction (**Fig. 7e,f**). At the broader functional-group level, withholding graminoid vegetation produced the largest and most

https://doi.org/10.5194/essd-2026-719
Preprint. Discussion started: 28 September 2026

consistent increase in MAE, whereas the mean performance loss associated with withholding woody vegetation was also substantial but varied strongly among folds. Exclusion of succulent vegetation or tidal-flat samples produced comparatively smaller changes. At the individual vegetation-type level, the largest deterioration occurred when Phragmites australis was absent from the training data, followed by mangroves and Suaeda spp. Withholding Scirpus spp. produced a moderate increase in error, whereas excluding Spartina spp. caused only a small change and withholding mixed-marsh samples produced little or no reduction in predictive performance. Together, these analyses show that the AlphaEarth-based model was relatively robust to training-sample reduction, PCD variation, and much of the observed VSRE range, while its extrapolation performance depended more strongly on whether structurally distinctive ecological groups were represented in the training support domain.

https://doi.org/10.5194/essd-2026-719
Preprint. Discussion started: 28 September 2026

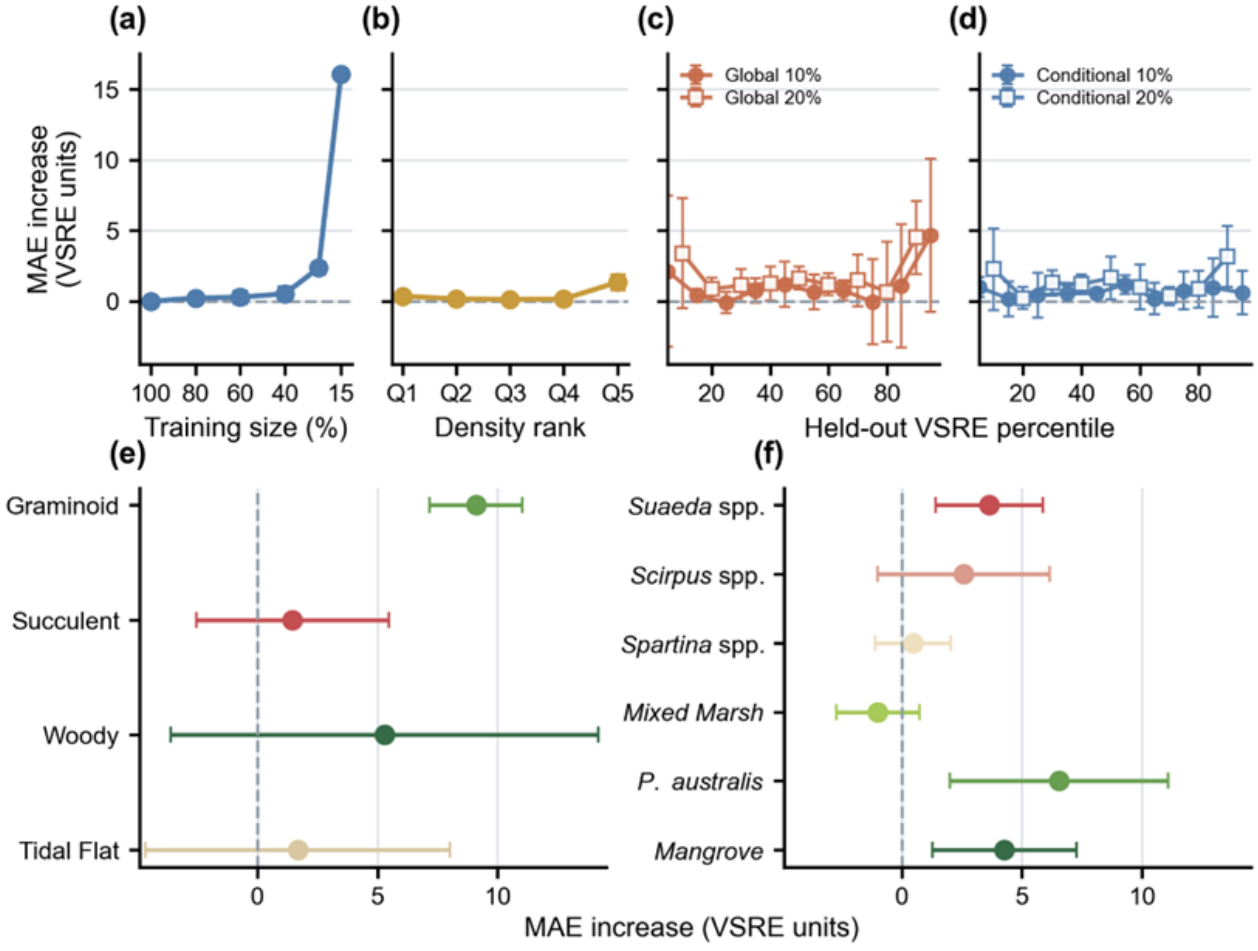

Fig. 7 | Sensitivity of VSRE prediction to training, acquisition and ecological support domains. a, Change in prediction MAE as the proportion of retained training samples decreases. **b**, Sensitivity to conditionally ranked point-cloud density classes. **c**,**d**, Changes in MAE after withholding globally (c) or conditionally (d) defined VSRE percentile ranges. Circles and open squares represent withheld 10% intervals and overlapping 20% intervals, respectively. e, Changes in MAE when individual vegetation functional types are excluded from the training support domain. f, Corresponding changes associated with unseen vegetation types. Points show mean MAE increases relative to the full-model baseline; error bars denote standard deviations across ten repeated subsampling runs in a and five spatial folds in b–f. The horizontal or vertical dashed line at zero indicates no change relative to the baseline, whereas positive values indicate reduced predictive performance.

1.3.5 Mapping wall-to-wall VSRE in coastal China

https://doi.org/10.5194/essd-2026-719
Preprint. Discussion started: 28 September 2026

Following model evaluation and robustness assessment, the final MLP model was fitted using all 1,273 quality-controlled LiDAR samples and applied to the 2022 AlphaEarth embeddings to generate a wall-to-wall VSRE map of coastal wetlands across China at 10 m spatial resolution (**Fig. 8**). Additionally, we compared species-level vegetation classification in the coastal zone with average EVI during the growing season (**Fig. 9**) (Qi et al., 2026).

Coastal vegetation composition varied substantially along the latitudinal gradient (**Fig. 8a**): mangrove communities dominated the low-latitude coast (20°–25°N), whereas Suaeda spp. and Phragmites australis were more prevalent at higher latitudes (35°–40°N). Mid-latitude regions (25°–35°N), particularly the Yangtze River Delta, contained more diverse vegetation assemblages and the largest extent of vegetated coastal wetlands.

The spatial distribution of VSRE revealed an additional structural gradient that was not fully represented by vegetation composition alone (**Fig. 8b**). Both the mean and spatial variability of VSRE generally decreased with increasing latitude. Major estuarine regions, including the Liaohe River Estuary, Yellow River Estuary, and Yangtze River Estuary, contained vegetation with relatively high VSRE and greater within-region variability compared with many smoother open-coast sections. This pattern was particularly evident in regions where multiple vegetation communities and geomorphic settings occurred within short spatial distances.

Fine-scale comparisons further showed substantial variation in VSRE within the same mapped vegetation type (**Fig. 9**). Areas assigned to a single vegetation class frequently contained pronounced internal structural gradients that were weakly represented by species identity or growing-season EVI alone. In several estuarine and wetland complexes, spatial differences in VSRE occurred within otherwise

https://doi.org/10.5194/essd-2026-719
Preprint. Discussion started: 28 September 2026

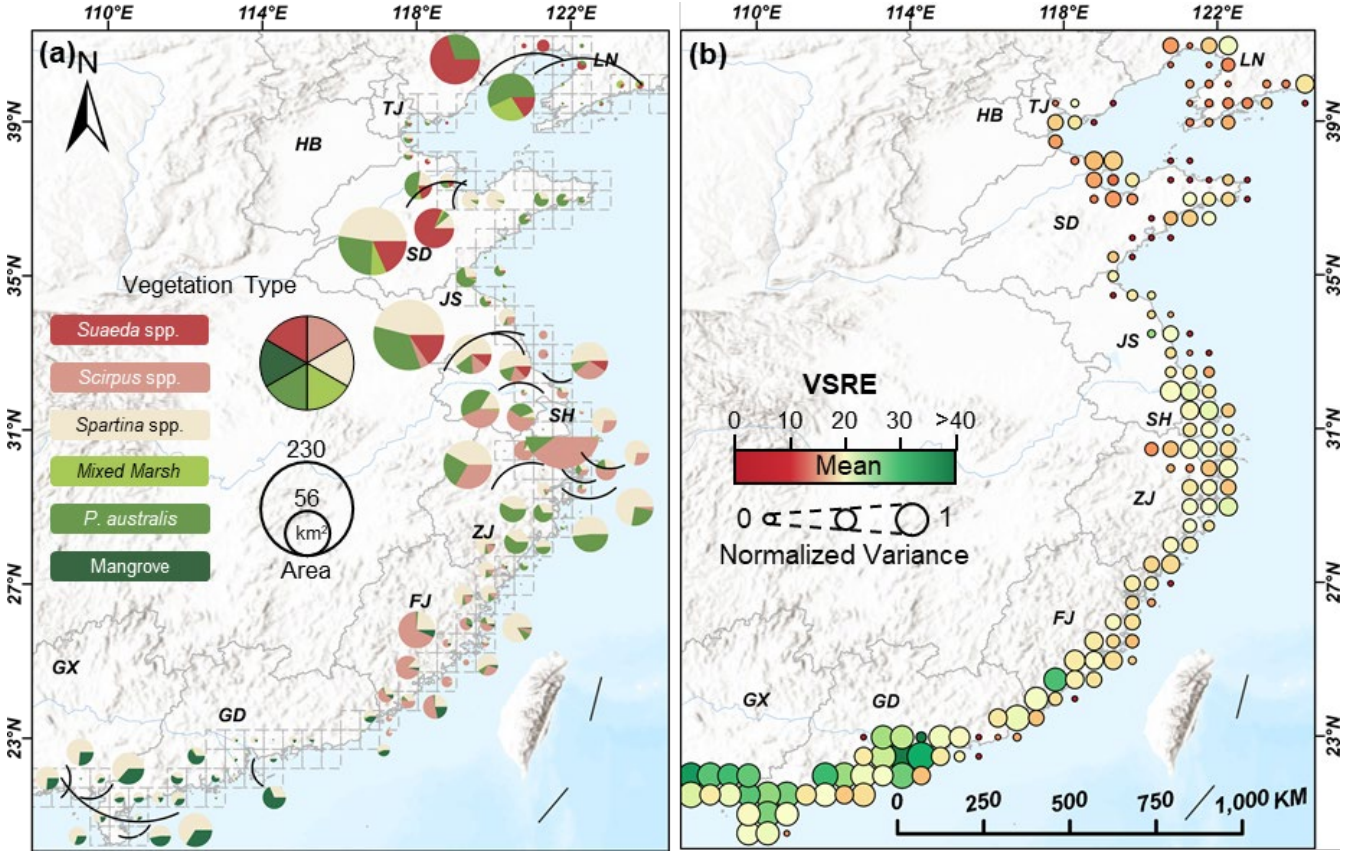

Fig. 8 | Spatial distribution of VSRE across coastal China. a, Vegetation composition across different coastal regions. The proportions of various vegetation types are illustrated using pie charts, with the sizes of the pie charts scaled to the total vegetation area within each 0.5° × 0.5° grid cell. **b**, Regional variation in VSRE. VSRE values are visualized using a color gradient from red (low complexity) to green (high complexity), while the circle sizes represent the normalized variance of VSRE within each 0.5° × 0.5° grid cell.

https://doi.org/10.5194/essd-2026-719
Preprint. Discussion started: 28 September 2026

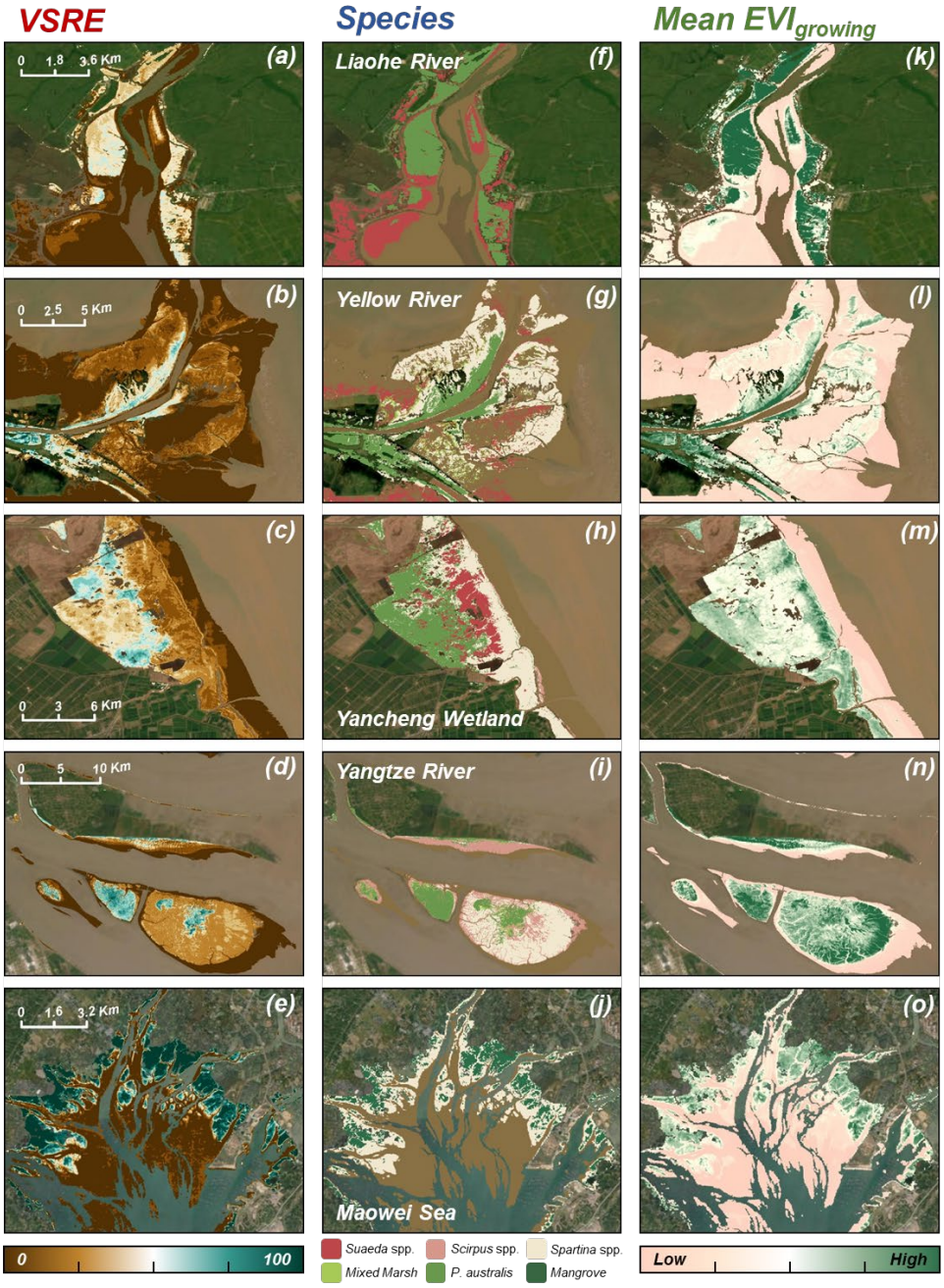

Fig. 9 | Comparison of VSRE with other widely used indicators for characterizing coastal wetlands. a-e, VSRE mapping, ranging from 0 to 100. **f-j,** main coastal vegetation mapping. **k-o,** mean growing-season EVI derived from Sentinel-2 optical imagery acquired in 2022, averaged from June to September (approximately ranging from 0 to 10).

1.3.6 Spatiotemporal dynamics of VSRE across coastal China

https://doi.org/10.5194/essd-2026-719
Preprint. Discussion started: 28 September 2026

Annual VSRE mapping revealed spatially heterogeneous but predominantly stable structural dynamics across China's coastal wetlands from 2017 to 2025 (**Fig. 10**). Among the 159 valid 0.5° coastal grid cells, 69.81% showed positive Sen's slopes and 30.19% showed negative slopes. However, only 6.29% and 5.03% of the grid cells exhibited significant increasing and decreasing trends, respectively, whereas 63.52% showed non-significant increases and 25.16% showed non-significant decreases (Mann–Kendall test, $P < 0.1$; **Fig. 10a**). Increasing and decreasing trends were spatially interspersed along the coastline, indicating that changes in coastal vegetation structure were primarily regional or local.

To characterize temporal changes in vegetation structure while minimizing confounding from vegetation-type transitions, we further selected 103,017 locations that were consistently classified as the same vegetation type throughout 2017–2022 and grouped them according to this stable pre-2023 classification (**Fig. 10c**). Their annual VSRE trajectories were then tracked from 2017 to 2025. Across these historically stable locations, the characteristic structural differences among vegetation types were broadly maintained through time. Mangrove locations consistently exhibited the highest VSRE, with annual mean values ranging from 43.20 to 51.05, whereas locations stably classified as *P. australis* during 2017–2022 remained within a relatively narrow range of 28.22–31.01 and those classified as *Suaeda* spp. ranged from 8.94 to 11.58. The coefficients of variation of annual mean VSRE were only 5.1%, 3.1%, and 8.0% for these three groups, respectively. This temporal consistency indicates that VSRE retained relatively stable structural signatures across locations with persistent vegetation composition during the period for which annual vegetation classifications were available.

A conspicuous departure from this pattern occurred at locations consistently classified as *Spartina* spp. during 2017–2022. Their mean VSRE decreased from 23.49 in 2023 to 21.81 in 2024 and 20.58 in

https://doi.org/10.5194/essd-2026-719
Preprint. Discussion started: 28 September 2026

2025, corresponding to a 12.4% decline over two years, while the median declined from 21.3 to 18.7 and then to 14.4. Because vegetation classifications after 2022 were unavailable, these locations were retained under their pre-2023 *Spartina* classification for temporal comparison. The abrupt structural decline coincided with the large-scale implementation of China's *Spartina alterniflora* removal program (Qi et al., 2024) and was spatially apparent in representative regions including the Yellow River Estuary and Jiuduansha (**Fig. 10b**). This temporal correspondence suggests that annual VSRE captured the structural loss and reorganization associated with large-scale vegetation removal, while the relative stability observed for most historically persistent vegetation groups illustrates its ability to characterize longer-lived structural properties.

https://doi.org/10.5194/essd-2026-719
Preprint. Discussion started: 28 September 2026

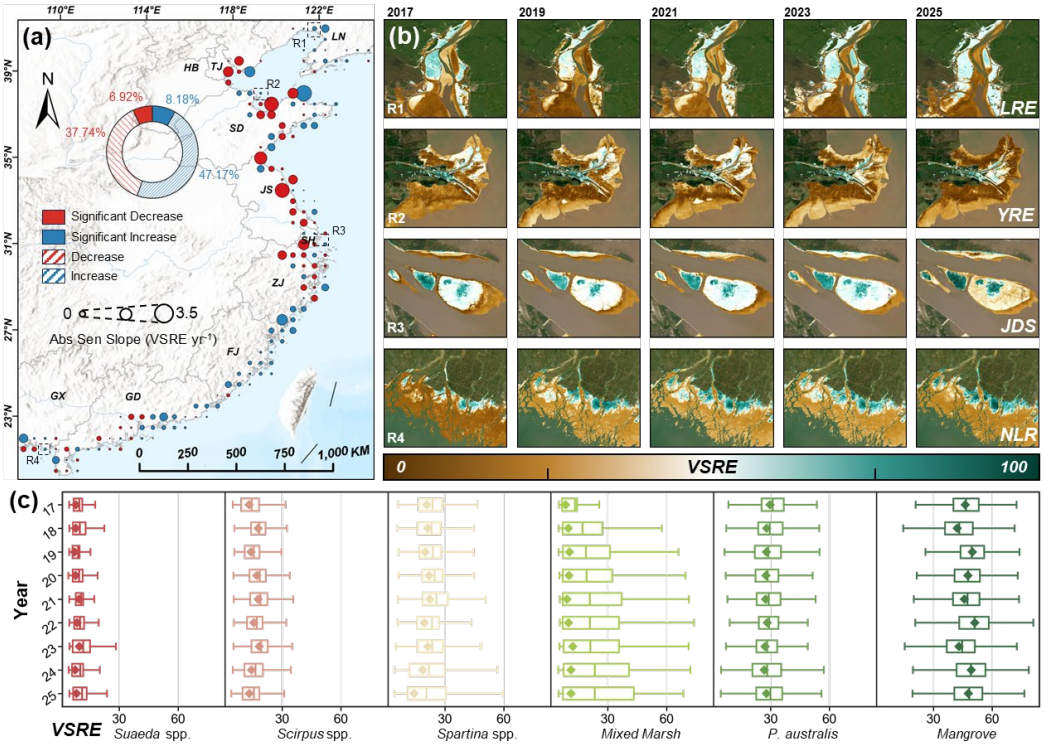

Fig. 10 | Spatiotemporal dynamics of VSRE across China's coastal wetlands. a, Spatial distribution of VSRE trends across 159 valid 0.5° coastal grid cells from 2017 to 2025. Symbol size is proportional to the absolute Sen's slope (VSRE yr^{-1}), whereas blue and red indicate increasing and decreasing trends, respectively. The inset summarizes the proportions of significant increases (6.29%), non-significant increases (63.52%), non-significant decreases (25.16%) and significant decreases (5.03%). Solid and hatched sectors represent significant and non-significant trends, respectively, with significance assessed using the Mann–Kendall test ($P < 0.1$). **b**, Spatial patterns of VSRE in four representative coastal wetland landscapes in 2017, 2019, 2021, 2023, and 2025. From top to bottom, the rows show the Liaohe River Estuary (LRE; R1), Yellow River Estuary (YRE; R2), Jiuduansha (JDS; R3), and Nanliu River Estuary (NLR; R4). Colors indicate VSRE values ranging from 0 to 100. **c,** Annual VSRE distributions from 2017 to 2025 for 103,017 locations with stable vegetation classifications during 2017–2022. Locations were retained only when they were consistently classified as the same vegetation type throughout the six-year period and were grouped according to that pre-2023 stable classification as *Spartina* spp., *Phragmites australis*, *Scirpus* spp., mixed marsh, *Suaeda* spp., or mangrove. Their VSRE values were subsequently tracked through 2025; because vegetation classifications were unavailable after 2022, the group labels for 2023–2025 denote historical vegetation identity rather than confirmed contemporaneous vegetation type. White boxes denote the interquartile range, whiskers extend to the most extreme values within 1.5 times the interquartile range, diamonds indicate medians, and vertical lines within boxes indicate means; outliers are not shown.

https://doi.org/10.5194/essd-2026-719
Preprint. Discussion started: 28 September 2026


Open Access Earth System Science Data Discussions

1.4 Discussion

1.4.1 Limitation of the information entropy-derived VSC index in coastal wetlands

The concept of entropy originates from physics, where it describes the degree of disorder within a system. Since Shannon introduced it into information theory, information entropy (IE) has been widely applied in digital information processing (Cover and Thomas, 1991). More recently, following previous work using IE (FHD, CE) to point cloud data to quantify forest canopy complexity (Liu et al., 2022), many studies have been conducted in-depth analyses of the ecological functions and structural characteristics of forest canopies based on this concept (Liu et al., 2024; De Conto et al., 2024; Wang et al., 2023).

However, when point-cloud IE is used directly as a proxy for VSC, an important conceptual limitation arises. In voxelized point clouds, IE primarily quantifies the evenness or uncertainty of point occupancy within predefined spatial units, such as voxels or height layers. It reaches its maximum when point occupancy is uniformly distributed and its minimum when points are concentrated in a small number of spatial units. Thus, high IE indicates uniform spatial occupancy, but such uniformity is not necessarily equivalent to ecological structural complexity. Mature forests provide an important case in which high IE may correspond well with high VSC, because canopy complementarity, vertical stratification, crown packing, trunks, understory vegetation, and gaps can jointly produce a saturated, spatially uniform point-cloud distribution. Yet IE does not distinguish between uniformity arising from complementary arrangements of diverse structural units and that arising from repetitive arrangements of simple structural units (**Fig. 11**).

This distinction is particularly important in coastal wetlands, where dense reed stands, Spartina alterniflora marshes, and other graminoid communities may consist of simple, repetitive structures yet

https://doi.org/10.5194/essd-2026-719
Preprint. Discussion started: 28 September 2026

exhibit uniform occupancy across voxels or height layers. In such cases, entropy-based metrics may overestimate VSC by interpreting dense, repetitive filling as structural complexity. Conversely, multispecies mixed communities may show lower global occupancy evenness but higher ecological VSC because their local structural configurations vary across space. Therefore, the relationship between entropy-based metrics and ecological VSC is context-dependent. **Supplementary Fig. 8** illustrates this potential mismatch and helps explain why the high-water-level group in our results showed lower ecological VSC but higher CE and FHD values than the medium-water-level group.

A further limitation of information-entropy-based metrics is their sensitivity to point cloud density and sampling distribution. Ideally, once point cloud density is sufficient to characterize vegetation three-dimensional structure, additional points should mainly reduce measurement noise rather than systematically alter the estimated VSC. However, IE is calculated from point-occupancy probabilities within voxels or height layers and therefore assumes that the observed point-cloud distribution accurately reflects the underlying vegetation structure. This assumption is often difficult to satisfy in LiDAR data, because point clouds are influenced by flight altitude, scan angle, return mode, canopy occlusion, sensor penetration, and surface reflectance. As point cloud density increases, newly added points may be disproportionately concentrated in upper canopies, outer surfaces, or high-reflectance regions rather than being distributed proportionally across all structural elements. In addition, IE has an upper bound determined by voxel size, vertical stratification, and plot extent; increasing point cloud density may fill more voxels and move the observed distribution toward this saturation limit. As a result, changes in IE may reflect a mixture of true structural variation, density effects, and sampling bias, rather than ecological structural complexity alone (**Fig. 11**).

https://doi.org/10.5194/essd-2026-719
Preprint. Discussion started: 28 September 2026

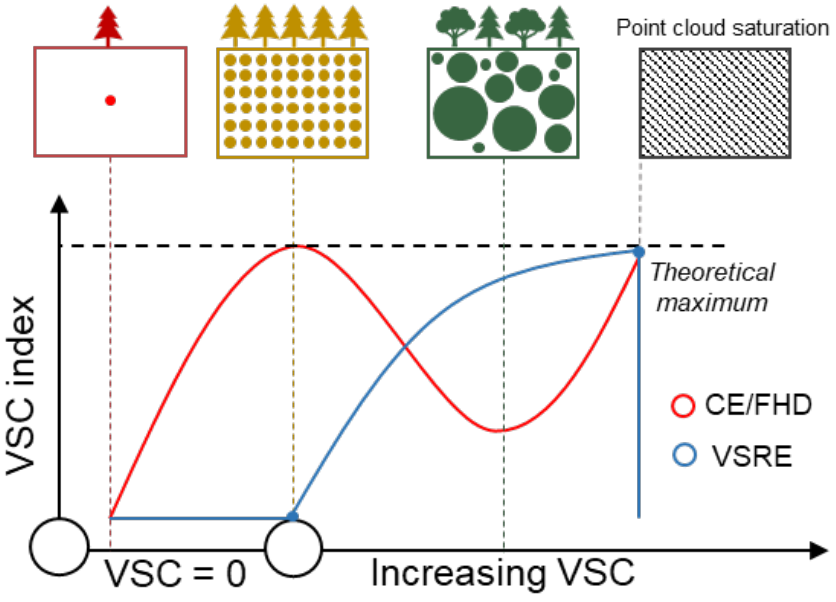

Fig. 11 | Theoretical trends of VSRE and CE/FHD as VSC increases.

1.4.2 Advantages of VSRE in coastal wetlands

RE differs from IE. Whereas IE quantifies the uncertainty or evenness of a single probability distribution, RE measures the divergence between probability distributions and directly quantifies their differences (Baez and Pollard, 2016). Based on this principle, VSRE does not primarily measure whether the entire plot space is uniformly filled. Instead, it uses regionalized point cloud data to construct normalized local voxel distributions using a three-dimensional sliding-window framework and compares spatial distribution differences across local windows. This design allows VSRE to assess the similarity among local structural configurations rather than global occupancy evenness.

When increased point cloud density mainly produces a more complete but similar sampling of the same structure, VSRE is not systematically inflated as IE is. For example, dense but repetitive monospecific communities may retain highly similar local configurations even at high point cloud density, whereas genuinely heterogeneous mixed communities show stronger differences in three-dimensional

https://doi.org/10.5194/essd-2026-719
Preprint. Discussion started: 28 September 2026

configurations among local windows. This mechanism aligns closely with our intuitive understanding of VSC: greater similarity among local structural configurations indicates lower configurational heterogeneity and therefore lower VSC.

Moreover, VSRE is computationally efficient. Rather than relying on kernel density estimation, resampling, or projection, VSRE performs discrete frequency statistics within voxelized boxes, thereby reducing computational cost while preserving the original three-dimensional structural information. In testing, VSRE was approximately 10 times faster than the CE algorithm for a single 25×25 m LiDAR sample, and this efficiency advantage increased with increasing point cloud density (**Supplementary Fig. 6**). This efficiency enables direct comparison of original point-cloud structural distributions and improves sensitivity to subtle local structural differences. Finally, VSRE provides adjustable parameters, particularly the vertical step size and maximum height in the Z direction, allowing users to fine-tune the metric for ecosystems with different structural traits, provided that the sample size is sufficient or point cloud densities are comparable in magnitude.

1.4.3 VSC of coastal wetlands in China

By deploying the VSRE algorithm across 1,337 LiDAR samples collected along coastal China and integrating species-level vegetation classification mapping, we achieved a comprehensive understanding of VSC at both the species and regional scales (**Figs. 5, 8 and 9, Supplementary Table 2**).

Our mapping revealed significant differences in VSC among coastal vegetation types, not only between different species but also within the same species across different regions. Differences in VSC among species may be attributed to variations in productivity, stress resistance, and growth cycles (Qi et al., 2024; Kirwan and Megonigal, 2013; Duarte et al., 2013; Mathis et al., 2024). Mangrove communities,

https://doi.org/10.5194/essd-2026-719
Preprint. Discussion started: 28 September 2026

characterized by high productivity and extended growth cycles (Rovai et al., 2018), exhibited higher VSC, while Scirpus spp. and Suaeda spp., which allocate more resources toward stress resistance, demonstrated relatively lower VSC (Lafond-Hudson and Sulman, 2023; Sun et al., 2022). Intraspecific differences in VSC appear to be influenced by local growth conditions and human disturbance. For example, *P. australis*, a species widely distributed along China's coast, exhibited the highest mean VSC in Shanghai ($VSRE_{mean}$ = 21.84), surpassing even the mangroves in Guangxi ($VSRE_{mean}$ = 20.92). It can be attributed to the dominance of *P. australis* in the long-protected Dongtan National Wetland in Shanghai, where favorable conditions support more structurally complex growth(Qi et al., 2024).

Additionally, the range of VSC within species is likely associated with the plants' intrinsic growth characteristics. Mangroves, with growth cycles of 5 to 10 years, can exhibit substantial structural variation among individuals of different ages, as in terrestrial forests, resulting in a wide range of VSRE values. In contrast, most salt marsh plants exhibit relatively simple, repetitive growth forms, resulting in unimodal frequency distributions of VSRE (Lafond-Hudson and Sulman, 2023). It is noteworthy that previous studies have shown that intertidal ecosystems often lack latitudinal diversity gradients (Thyrring and Harley, 2024), a conclusion supported by our coastal vegetation species mapping (**Fig. 8a**). However, VSC, as characterized by VSRE, exhibits a clear latitudinal gradient in both mean and variance (**Fig. 8b**). This discrepancy suggests that structural complexity may be a more suitable and universally applicable functional characteristic for both terrestrial and marine ecosystems.

1.4.4 Limitations and Uncertainties

Although VSRE offers significant advantages in theoretical interpretability and computational efficiency, several limitations should be acknowledged. First, VSRE requires a high degree of information fidelity

https://doi.org/10.5194/essd-2026-719
Preprint. Discussion started: 28 September 2026

in the input point cloud. Specifically, the spatial distribution of points should accurately represent the actual three-dimensional vegetation structure, with limited distortion from sampling methods or external factors. A major challenge in applying VSRE to airborne or satellite-borne LiDAR data is the potential information distortion caused by dense canopy cover, which can reduce laser penetration and bias the observed point distribution (Wulder et al., 2012). In this study, the application of VSRE to coastal wetlands, where vegetation canopies are generally more open than closed forests, reduces but does not eliminate this concern.

Second, VSRE should be interpreted as an index that primarily captures spatial configurational heterogeneity rather than the total area of occupied vegetation. In a broad ecological sense, vegetation structural complexity may include both spatial occupancy and spatial heterogeneity (Coverdale and Davies, 2023). VSRE is more closely aligned with the latter because it compares differences among local voxel-based structural distributions. Therefore, in structurally more complex ecosystems or in mature ecosystems where vegetation space is nearly saturated, VSRE alone may not fully capture all dimensions of structural complexity. In such cases, combining VSRE with complementary metrics such as canopy cover, vegetation height, or a spatial occupancy index (Zhao et al., 2026) would provide a more complete characterization of VSC.

Third, RE-based algorithms have theoretical limitations, although these conditions are rarely encountered in natural ecosystems. When vegetation structures become extremely saturated and local point-cloud distributions within windows become highly similar, RE values may decrease toward zero because little distributional divergence remains across windows. In addition, when structures consist of simple rearrangements of identical elements, such as repeated clusters of uniform vegetation point clouds

https://doi.org/10.5194/essd-2026-719
Preprint. Discussion started: 28 September 2026

distributed across space, RE may be unable to distinguish them if their normalized voxel distributions are effectively equivalent. These limitations indicate that VSRE is most informative when structural complexity is expressed as local configurational heterogeneity rather than as uniform saturation or repeated relocation of identical structural units.

Finally, though VSRE remains relatively insensitive to point-cloud density, we recommend using LiDAR datasets with comparable point-cloud densities, preferably greater than 250 pt m^{-2}, to ensure reliable comparisons among samples or ecosystems.

2 Data availability

The data products and supporting materials described in this manuscript are archived in Figshare under a CC BY 4.0 licence (Qi et al., 2026). During peer review, the repository is accessible through the anonymous review link: https://figshare.com/s/0a1ee71507b803b508e2. Upon publication, the repository will be released publicly with a persistent DOI, which should be used when citing the dataset.

The Figshare archive provides the complete data package supporting ChinaTidalVSC. It includes: (1) nine annual wall-to-wall VSRE maps of China's coastal tidal wetlands from 2017 to 2025 at a nominal spatial resolution of 10 m; (2) a quality-controlled sample-level dataset containing 1,273 coastal vegetation observations, including geographic coordinates, vegetation and functional types, point-cloud density, LiDAR-derived reference VSRE, model-predicted VSRE, and the corresponding 64-dimensional AlphaEarth Foundation features; (3) geographic representations of the field-sample locations; (4) 53 standardized 25 × 25 m fixed-field LiDAR samples in LAS format together with their corresponding spatial boundaries; and (5) documentation describing file organization, variable definitions, coordinate reference systems, scaling conventions, missing-value rules, and recommended use.

https://doi.org/10.5194/essd-2026-719
Preprint. Discussion started: 28 September 2026

The annual VSRE rasters are stored as UInt16 GeoTIFFs in EPSG:4326. Valid raster values represent VSRE × 10 and should therefore be divided by 10 to recover the original dimensionless VSRE values; 65535 represents NoData. The sample-level table and accompanying data dictionary provide the definitions and units of all ecological, LiDAR, AEF, and VSRE variables. The released LAS files are standardized sample-scale derivatives intended to support inspection and methodological reuse of the LiDAR structural information; the complete flight-scale UAV-LiDAR datasets are not redistributed as part of the present archive.

For convenient browser-based access to the annual spatial products, we additionally provide a Google Earth Engine application ([https://planar-maxim-362707.projects.earthengine.app/view/chinatidalvscexplorer]). The application allows users to visualize and access the annual ChinaTidalVSC products without locally processing the full raster archive.

Detailed descriptions of the data structure, variable definitions, recommended workflows, and usage considerations are provided in the README and data dictionary accompanying the Figshare archive. Third-party input datasets used to generate ChinaTidalVSC, including AlphaEarth Foundation embeddings and other Earth-observation products, are cited in the manuscript and are not redistributed where redistribution is restricted by the original data providers.

3 Code availability

The source code used to calculate VSRE and perform AlphaEarth-based spatial inference is openly available through GitHub at https://github.com/EmpTyset-phi/VSRE. The repository contains the implementation used for VSRE calculation and the associated inference workflow and will be maintained as the version-controlled development repository for the method.

https://doi.org/10.5194/essd-2026-719
Preprint. Discussion started: 28 September 2026

To facilitate use by researchers without a programming environment, a standalone Windows graphical user interface (GUI) that packages the same VSRE implementation is also provided in the Figshare data archive. The GUI supports VSRE calculation from compatible LiDAR LAS files and model-based VSRE inference from 64-band AEF input data. The Figshare archive therefore provides a fixed release associated with the published dataset, while GitHub provides the maintained source-code repository.

4 Conclusions

Drawing on the world's largest water-level control experiment and the most comprehensive LiDAR dataset of China's coastal zone, this study developed the VSRE index based on the concept of RE to effectively quantify the complexity of coastal VSC. Compared to the currently used VSC index, VSRE offers clear advantages in theoretical foundation, computational efficiency, and range of application. It enables the detailed characterization of VSC within coastal plant communities. Our findings advance the understanding of growth characteristics in coastal vegetation and provide an essential scientific basis for developing sustainable coastal management policies. Furthermore, given the critical ecosystem services they provide, this study underscores the urgent need to address the underrepresentation of coastal wetlands in current land-surface models.

https://doi.org/10.5194/essd-2026-719
Preprint. Discussion started: 28 September 2026

Supplementary Materials

Supplementary Materials are available for this paper, including Figures S1 to S9, Tables S1 to S4 and texts S1-S3. The link to the supplement will be included by Copernicus.

Author contributions

J.M. and X.C. conceived the idea. G.P.Q., J.W.W., Z.Z.X., L.C.Y. and H.L.Y. performed the research. G.P.Q. and J.W.W. analyzed the data and made the visualizations. G.P.Q. and J.W.W. wrote the first draft with help from J.M., X.C., B.L. and M.N..

Competing interests

The authors declare no competing interests.

Acknowledgements

We sincerely thank Keryn Gedan from George Washington University for her contribution to improving the first draft. We also acknowledge the support and assistance from the CFFF Intelligent Computing Platform at Fudan University.

Financial support

This research was supported by the Natural Science Foundation of China (32672105, 32271659), the Scientific Research Program of Shanghai Science and Technology Commission (23DZ1204504), State Key Laboratory of Wetland Conservation and Restoration-Wetland Young Scientist Program (SDGZ-QN2025-03), the Fundamental and Interdisciplinary Disciplines Breakthrough Plan of the Ministry of Education of China (NO.JYB2025XDXM911), and the Open funding project from the state key laboratory for vegetation structure, function and construction (VegLabOF2025005).

https://doi.org/10.5194/essd-2026-719
Preprint. Discussion started: 28 September 2026

References

Atkins, J. W., Bohrer, G., Fahey, R. T., Hardiman, B. S., Morin, T. H., Stovall, A. E., Zimmerman, N., and Gough, C. M.: Quantifying vegetation and canopy structural complexity from terrestrial Li DAR data using the forestr r package, Methods Ecol. Evol., 9, 2057-2066, 2018.

Baez, J. C. and Pollard, B. S.: Relative entropy in biological systems, Entropy, 18, 46, 2016.

Bergen, K., Goetz, S., Dubayah, R., Henebry, G., Hunsaker, C., Imhoff, M., Nelson, R., Parker, G., and Radeloff, V.: Remote sensing of vegetation 3 ‐ D structure for biodiversity and habitat: Review and implications for lidar and radar spaceborne missions, J. Geophys. Res.: Biogeosci., 114, 2009.

Brown, C. F., Kazmierski, M. R., Pasquarella, V. J., Rucklidge, W. J., Samsikova, M., Zhang, C., Shelhamer, E., Lahera, E., Wiles, O., and Ilyushchenko, S.: AlphaEarth Foundations: An embedding field model for accurate and efficient global mapping from sparse label data, arXiv preprint arXiv:2507.22291, 2025.

Chambers, J. Q., Asner, G. P., Morton, D. C., Anderson, L. O., Saatchi, S. S., Espírito-Santo, F. D., Palace, M., and Souza, C.: Regional ecosystem structure and function: ecological insights from remote sensing of tropical forests, Trends Ecol. Evol., 22, 414-423, 2007.

Chen, H., Covert, I. C., Lundberg, S. M., and Lee, S.-I.: Algorithms to estimate Shapley value feature attributions, Nat. Mach. Intell., 5, 590-601, 2023.

Costanza, R., d'Arge, R., De Groot, R., Farber, S., Grasso, M., Hannon, B., Limburg, K., Naeem, S., O'neill, R. V., and Paruelo, J.: The value of the world's ecosystem services and natural capital, Nature, 387, 253-260, 1997.

Cousins, S. H.: Species diversity measurement: choosing the right index, Trends Ecol. Evol., 6, 190-192, 1991.

Cover, T. M. and Thomas, J. A.: Entropy, relative entropy and mutual information, Elements of information theory, 2, 12-13, 1991.

Coverdale, T. C. and Davies, A. B.: Unravelling the relationship between plant diversity and vegetation structural complexity: A review and theoretical framework, J. Ecol., 111, 1378-1395, 2023.

Dassot, M., Constant, T., and Fournier, M.: The use of terrestrial LiDAR technology in forest science: application fields, benefits and challenges, Ann. For. Sci., 68, 959-974, 2011.

de Conto, T., Armston, J., and Dubayah, R.: Characterizing the structural complexity of the Earth's forests with spaceborne lidar, Nat. Commun., 15, 8116, 2024.

Dobson, J. E.: NOAA Coastal Change Analysis Program (C-CAP): guidance for regional implementation, 1995.

Duarte, C. M., Losada, I. J., Hendriks, I. E., Mazarrasa, I., and Marbà, N.: The role of coastal plant communities for climate change mitigation and adaptation, Nat. Clim. Change, 3, 961-968, 10.1038/nclimate1970, 2013.

Ehbrecht, M., Seidel, D., Annighöfer, P., Kreft, H., Köhler, M., Zemp, D. C., Puettmann, K., Nilus, R., Babweteera, F., and Willim, K.: Global patterns and climatic controls of forest structural complexity, Nat. Commun., 12, 519, 2021.

Fick, S. E. and Hijmans, R. J.: WorldClim 2: new 1 ‐ km spatial resolution climate surfaces for global land areas, Int. J.

https://doi.org/10.5194/essd-2026-719
Preprint. Discussion started: 28 September 2026

Climatol., 37, 4302-4315, 2017.

Fischer, F. J., Maréchaux, I., and Chave, J.: Improving plant allometry by fusing forest models and remote sensing, New Phytol., 223, 1159-1165, 2019.

Guo, Q., Su, Y., Hu, T., Guan, H., Jin, S., Zhang, J., Zhao, X., Xu, K., Wei, D., and Kelly, M.: Lidar boosts 3D ecological observations and modelings: A review and perspective, IEEE Geosci. Remote Sens. Mag., 9, 232-257, 2020.

He, Q., Li, Z. a., Daleo, P., Lefcheck, J. S., Thomsen, M. S., Adams, J. B., and Bouma, T. J.: Coastal wetland resilience through local, regional and global conservation, Nat. Rev. Biodivers., 1, 50-67, 10.1038/s44358-024-00004-x, 2025.

Holling, C. S.: Simplifying the complex: the paradigms of ecological function and structure, Eur. J. Oper. Res., 30, 139-146, 1987.

Jucker, T., Fischer, F. J., Chave, J., Coomes, D. A., Caspersen, J., Ali, A., Loubota Panzou, G. J., Feldpausch, T. R., Falster, D., and Usoltsev, V. A.: Tallo: A global tree allometry and crown architecture database, Global Change Biol., 28, 5254-5268, 2022.

Keller, M., Schimel, D. S., Hargrove, W. W., and Hoffman, F. M.: A continental strategy for the National Ecological Observatory Network, The Ecological Society of America: 282-284, 2008.

Kirwan, M. L. and Megonigal, J. P.: Tidal wetland stability in the face of human impacts and sea-level rise, Nature, 504, 53-60, 10.1038/nature12856, 2013.

Krishnan, S., Crosby, C., Nandigam, V., Phan, M., Cowart, C., Baru, C., and Arrowsmith, R.: OpenTopography: a services oriented architecture for community access to LIDAR topography, Proceedings of the 2nd international conference on computing for Geospatial Research & Applications, 1-8,

Kulp, S. A. and Strauss, B. H.: CoastalDEM: A global coastal digital elevation model improved from SRTM using a neural network, Remote Sens. Environ., 206, 231-239, 2018.

LaFond‐Hudson, S. and Sulman, B.: Modeling strategies and data needs for representing coastal wetland vegetation in land surface models, New Phytol., 238, 938-951, 10.1111/nph.18760, 2023.

Liu, X., Ma, Q., Wu, X., Hu, T., Liu, Z., Liu, L., Guo, Q., and Su, Y.: A novel entropy-based method to quantify forest canopy structural complexity from multiplatform lidar point clouds, Remote Sens. Environ., 282, 113280, 2022.

Liu, X., Feng, Y., Hu, T., Luo, Y., Zhao, X., Wu, J., Maeda, E. E., Ju, W., Liu, L., and Guo, Q.: Enhancing ecosystem productivity and stability with increasing canopy structural complexity in global forests, Sci. Adv., 10, eadl1947, 2024.

Lohani, B. and Ghosh, S.: Airborne LiDAR technology: A review of data collection and processing systems, Proc. Natl. Acad. Sci., India, Sect. A Phys. Sci., 87, 567-579, 2017.

Loreau, M., Naeem, S., Inchausti, P., Bengtsson, J., Grime, J. P., Hector, A., Hooper, D. U., Huston, M. A., Raffaelli, D., Schmid, B., Tilman, D., and Wardle, D. A.: Biodiversity and ecosystem functioning: current knowledge and future challenges, Science, 294, 804-808, 10.1126/science.1064088, 2001.

MacArthur, R. H. and MacArthur, J. W.: On bird species diversity, Ecology, 42, 594-598, 1961.

Mathis, M., Lacroix, F., Hagemann, S., Nielsen, D. M., Ilyina, T., and Schrum, C.: Enhanced CO2 uptake of the coastal ocean is dominated by biological carbon fixation, Nat. Clim. Change, 14, 373-379, 2024.

https://doi.org/10.5194/essd-2026-719
Preprint. Discussion started: 28 September 2026

Mcleod, E., Chmura, G. L., Bouillon, S., Salm, R., Björk, M., Duarte, C. M., Lovelock, C. E., Schlesinger, W. H., and Silliman, B. R.: A blueprint for blue carbon: toward an improved understanding of the role of vegetated coastal habitats in sequestering CO2, Front. Ecol. Environ., 9, 552-560, 10.1890/110004, 2011.

Moffett, K. B., Nardin, W., Silvestri, S., Wang, C., and Temmerman, S.: Multiple stable states and catastrophic shifts in coastal wetlands: Progress, challenges, and opportunities in validating theory using remote sensing and other methods, Remote Sens., 7, 10184-10226, 2015.

Morsdorf, F., Meier, E., Kötz, B., Itten, K. I., Dobbertin, M., and Allgöwer, B.: LIDAR-based geometric reconstruction of boreal type forest stands at single tree level for forest and wildland fire management, Remote Sens. Environ., 92, 353-362, 2004.

Parker, G. G. and Russ, M. E.: The canopy surface and stand development: assessing forest canopy structure and complexity with near-surface altimetry, For. Ecol. Manage., 189, 307-315, 2004.

Pinkus, A.: Approximation theory of the MLP model in neural networks, Acta Numer., 8, 143-195, 1999.

Qi, G., Wei, J., Li, H., Xie, T., Li, L., Wang, F., He, Q., Mudd, S. M., and Ma, J.: Insight into rapid vegetation dynamics in China's saltmarshes reveals overlooked coastal soil carbon storage, One Earth, 9, 2026.

Qi, G., Li, L., Li, H., Liu, Y., Xie, T., Guo, H., Ma, Z., Wu, J., Li, B., and Ma, J.: Ecological Effects of the Huge Invasive Species Removal Project in Coastal China, Environ. Sci. Technol., 2024.

Qi, Guanpu; Wei, Jiawei; Xin, Zaizhou; Yao, Longcheng; Chen, Xiong; Ma, Jun (2026). VSRE mapping data for "Revealing coastal vegetation structural diversity through LiDAR-derived relative entropy". figshare. Dataset. https://doi.org/10.6084/m9.figshare.30588722

Rahman, M.: Physically Interpretable AlphaEarth Foundation Model Embeddings Enable LLM-Based Land Surface Intelligence, 2026.

Robinson, C. J., Bohannan, B. J., and Young, V. B.: From structure to function: the ecology of host-associated microbial communities, Microbiol. Mol. Biol. Rev., 74, 453-476, 2010.

Rovai, A. S., Twilley, R. R., Castañeda-Moya, E., Riul, P., Cifuentes-Jara, M., Manrow-Villalobos, M., Horta, P. A., Simonassi, J. C., Fonseca, A. L., and Pagliosa, P. R.: Global controls on carbon storage in mangrove soils, Nat. Clim. Change, 8, 534-538, 10.1038/s41558-018-0162-5, 2018.

Sun, B., Jiang, M., Han, G., Zhang, L., Zhou, J., Bian, C., Du, Y., Yan, L., and Xia, J.: Experimental warming reduces ecosystem resistance and resilience to severe flooding in a wetland, Sci. Adv., 8, eabl9526, 10.1126/sciadv.abl9526, 2022.

Taddeo, S., Dronova, I., and Depsky, N.: Spectral vegetation indices of wetland greenness: Responses to vegetation structure, composition, and spatial distribution, Remote Sens. Environ., 234, 111467, 2019.

Tang, H., Armston, J., Hancock, S., Marselis, S., Goetz, S., and Dubayah, R.: Characterizing global forest canopy cover distribution using spaceborne lidar, Remote Sens. Environ., 231, 111262, 2019.

Temmerman, S., Meire, P., Bouma, T. J., Herman, P. M., Ysebaert, T., and De Vriend, H. J.: Ecosystem-based coastal defence

https://doi.org/10.5194/essd-2026-719
Preprint. Discussion started: 28 September 2026

in the face of global change, Nature, 504, 79-83, 10.1038/nature12859, 2013.

Theiler, J.: Estimating fractal dimension, Journal of the optical society of America A, 7, 1055-1073, 1990.

Thyrring, J. and Harley, C. D.: Marine latitudinal diversity gradients are generally absent in intertidal ecosystems, Ecology, 105, e4205, 2024.

Wang, X., Rahman, M. A., Mokroš, M., Rötzer, T., Pattnaik, N., Pang, Y., Zhang, Y., Da, L., and Song, K.: The influence of vertical canopy structure on the cooling and humidifying urban microclimate during hot summer days, Landscape Urban Plann., 238, 104841, 2023.

Weilhoefer, C.: A review of indicators of estuarine tidal wetland condition, Ecol. Indic., 11, 514-525, 2011.

Wulder, M. A., White, J. C., Nelson, R. F., Næsset, E., Ørka, H. O., Coops, N. C., Hilker, T., Bater, C. W., and Gobakken, T.: Lidar sampling for large-area forest characterization: A review, Remote Sens. Environ., 121, 196-209, 2012.

Yando, E. S., Jones, S. F., James, W. R., Colombano, D. D., Montemayor, D. I., Nolte, S., Raw, J. L., Ziegler, S. L., Chen, L., and Daffonchio, D.: An integrative salt marsh conceptual framework for global comparisons, Limnol. Oceanogr. Lett., 8, 830-849, 10.1002/lol2.10346, 2023.

Yu, J., Nie, S., Liu, W., Sun, Z., Wang, C., Xi, X., Zhu, X., and Fang, M.: Evaluating and comparing the performance of ICESat-2 and GEDI data for estimating aboveground biomass in mangroves, Int. J. Digital Earth, 19, 2627082, 2026.

Zhao, Y., Zhen, Z., Zhang, Z., Guan, X., Wang, J., and Zhao, Y.: Spatial occupancy index of tree crown: Can provide new perspectives for quantifying structural complexity of individual tree crowns, Remote Sens. Environ., 335, 115277, 2026.